Cell

Infection trains the host for microbiota-enhanced resistance to pathogens

Graphical Abstract

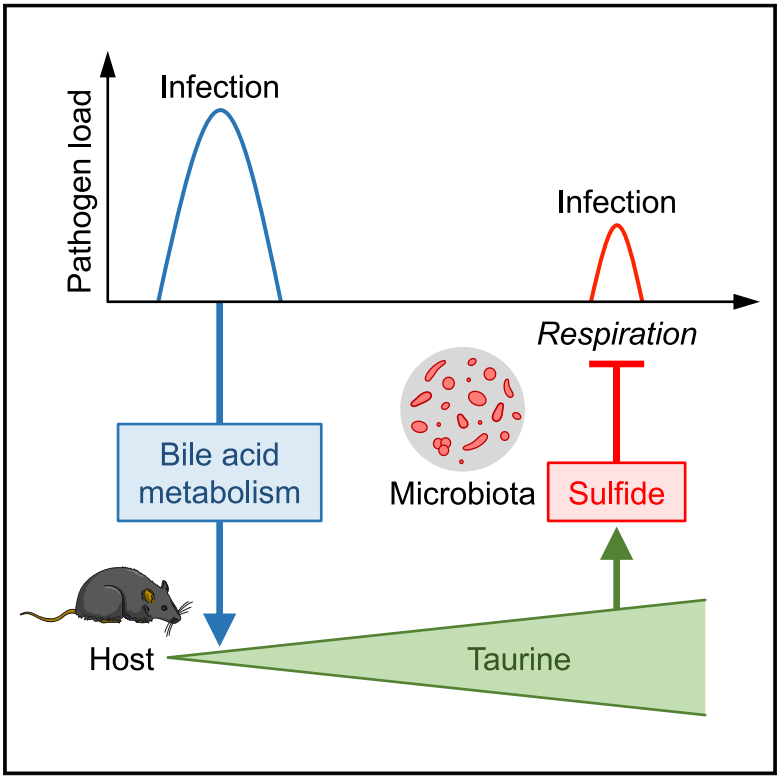

Authors

Apollo Stacy, Vinicius Andrade-Oliveira, John A. McCulloch, ..., Julia A. Segre, Barbara Rehermann, Yasmine Belkaid

Correspondence

apollo.stacy@nih.gov (A.S.), ybelkaid@niaid.nih.gov (Y.B.)

In Brief

Previous intestinal infection increases the gut microbiota's resistance to subsequent infection by inhibiting the ability of pathogens to respire.

Highlights

- Prior gut infection increases the microbiota's resistance to subsequent infection
- Infection induces host taurine production and the expansion of taurine utilizers
- The gut microbiota converts taurine to sulfide, inhibiting pathogen respiration
- Sulfide sequestration unleashes endogenous respirers in the gut microbiota

Stacy et al., 2021, Cell *184*, 615–627
February 4, 2021 Published by Elsevier Inc.
https://doi.org/10.1016/j.cell.2020.12.011

Cell

CellPress

Article

Infection trains the host for microbiota-enhanced resistance to pathogens

Apollo Stacy,[1,2,3,*] Vinicius Andrade-Oliveira,[1,7] John A. McCulloch,[4] Benedikt Hild,[5] Ji Hoon Oh,[5] P. Juliana Perez-Chaparro,[2] Choon K. Sim,[6,8] Ai Ing Lim,[1] Verena M. Link,[1] Michel Enamorado,[1] Giorgio Trinchieri,[4] Julia A. Segre,[6] Barbara Rehermann,[5] and Yasmine Belkaid[1,2,9,*]

[1]Metaorganism Immunity Section, Laboratory of Host Immunity and Microbiome, National Institute of Allergy and Infectious Diseases, National Institutes of Health, Bethesda, MD 20892, USA

[2]NIAID Microbiome Program, National Institute of Allergy and Infectious Diseases, National Institutes of Health, Bethesda, MD 20892, USA

[3]Postdoctoral Research Associate Training Program, National Institute of General Medical Sciences, National Institutes of Health, Bethesda, MD 20892, USA

[4]Laboratory of Integrative Cancer Immunology, Center for Cancer Research, National Cancer Institute, National Institutes of Health, Bethesda, MD 20892, USA

[5]Immunology Section, Liver Diseases Branch, National Institute of Diabetes and Digestive and Kidney Diseases, National Institutes of Health, Bethesda, MD 20892, USA

[6]Microbial Genomics Section, Translational and Functional Genomics Branch, National Human Genome Research Institute, National Institutes of Health, Bethesda, MD 20892, USA

[7]Present address: Center for Natural and Human Sciences, Federal University of ABC (UFABC), Santo André-SP, Brazil

[8]Present address: Singapore Institute for Clinical Sciences, Agency for Science, Technology and Research (A*STAR), Singapore, Singapore

[9]Lead contact

*Correspondence: apollo.stacy@nih.gov (A.S.), ybelkaid@niaid.nih.gov (Y.B.)

https://doi.org/10.1016/j.cell.2020.12.011

SUMMARY

The microbiota shields the host against infections in a process known as colonization resistance. How infections themselves shape this fundamental process remains largely unknown. Here, we show that gut microbiota from previously infected hosts display enhanced resistance to infection. This long-term functional remodeling is associated with altered bile acid metabolism leading to the expansion of taxa that utilize the sulfonic acid taurine. Notably, supplying exogenous taurine alone is sufficient to induce this alteration in microbiota function and enhance resistance. Mechanistically, taurine potentiates the microbiota's production of sulfide, an inhibitor of cellular respiration, which is key to host invasion by numerous pathogens. As such, pharmaceutical sequestration of sulfide perturbs the microbiota's composition and promotes pathogen invasion. Together, this work reveals a process by which the host, triggered by infection, can deploy taurine as a nutrient to nourish and train the microbiota, promoting its resistance to subsequent infection.

INTRODUCTION

The microbiota of host metaorganisms presents a formidable barrier to invasion by pathogens. Highlighting this, collateral damage to the microbiota by antibiotic therapy is often followed by the expansion of highly intractable antibiotic-resistant pathogens. Globally, antibiotic-resistant pathogens kill over 700,000 people per year, and over the next several decades, are expected to continue to represent a major cause of worldwide mortality (United Nations Interagency Coordination Group on Antimicrobial Resistance, 2019). For this reason, it is imperative to develop strategies to sustain or improve host antimicrobial defenses. One such arm of metaorganism immunity is colonization resistance, or the ability of the microbiota to resist pathogen colonization. Colonization resistance comprises via numerous inhibitory mechanisms that can be either direct or indirect/host mediated (Kim et al., 2017). The factors controlling colonization resistance, as well as the multiple mechanisms associated with this fundamental function, still remain to be fully explored.

A defining feature underlying the evolutionary success of the immune system is its ability to develop both innate and adaptive memory against pathogens, promoting more rapid and robust host responses to subsequent infections. Though memory was once exclusively attributed to the adaptive immune system, it is now appreciated that the innate immune system can also be trained to fully mature and attain enhanced function (Netea et al., 2020). Moreover, maturation of the adaptive and innate immune systems results not only through infections but, beginning in infancy, also through numerous other exposures such as diet and the microbiota (Macpherson et al., 2017). Whether host memory of previous encounters reciprocally shapes the microbiota remains unclear.

The microbiota like the immune system is highly dynamic. Notably, age-associated shifts in the microbiota strongly

influence the microbiota's functional capacity and host fitness (Stewart et al., 2018). A key example is that the immature microbiota of neonates is highly susceptible to pathogen invasion (Singer et al., 2019). Factors that modulate the development and maintenance of the microbiota include cross-talk with the immune system (McLoughlin et al., 2016), antibiotic exposure (Roubaud-Baudron et al., 2019), and defined dietary components (Wotzka et al., 2019). Increasingly appreciated is also the role of pathogens in remodeling the microbiota (Kamdar et al., 2016; Molloy et al., 2013). For instance, by eliciting an overly exuberant immune response, pathogens can gain access to inflammatory byproducts, such as elevated oxygen in normally anaerobic niches, that enable utilization of non-fermentable, strictly respiratory substrates for growth (Lopez et al., 2016).

Due to the prevalence of infections throughout evolution, we hypothesize that host metaorganisms have adapted strategies to harness infection-elicited microbiota for their own benefit and greater defense against subsequent infection. A corollary of this hypothesis is that regular exposure to pathogens may be beneficial for the microbiota to develop optimal antimicrobial function. In industrialized societies, however, improved hygiene and sanitation is thought to have reduced exposure to certain classes of pathogens, contributing to a recent precipitous decline in microbiota diversity and beneficial functions (Sonnenburg and Sonnenburg, 2019; Ramanan et al., 2016). Aligning with this, studies with the microbiota of wild and pet-shop mice (Beura et al., 2016; Rosshart et al., 2017, 2019), which inevitably encounter more infections than their laboratory counterparts, have demonstrated that mice with a history of infection exhibit altered immunity (Reese et al., 2016) and heightened resistance to perturbations of their gut microbiota (Rosshart et al., 2019).

Here, we examined the possibility that prior infections could enhance metaorganism colonization resistance and that dissecting the underlying molecular mechanism would lead to the identification of novel microbiota-directed therapeutics. Our results uncover that the host, triggered by transient infection, deploys the sulfonic acid taurine as a nutrient to promote long-term resistance of the microbiota to subsequent infection.

RESULTS

Infection-trained microbiota enhance colonization resistance

To assess the impact of infection on the ability of the microbiota to promote colonization resistance, we first sought a model pathogen whose colonization of the host is dictated primarily by the microbiota. We therefore chose the hospital-associated pathogen *Klebsiella pneumoniae* (*Kpn*) (Centers for Disease Control and Prevention, 2019), specifically a derivative of a carbapenem-resistant clinical isolate (Ramage et al., 2017). Though extraintestinal infections with *Kpn* can be life threatening, otherwise healthy individuals can harbor *Kpn* at low levels in their gut microbiota, and hospitalized patients colonized with *Kpn* are at much greater risk for subsequent systemic infection (Conlan et al., 2016; Gorrie et al., 2017). In mice, following oral infection with a high dose, *Kpn* can be transiently detected in the lumen of the large intestine before it is no longer detectable in the stool by 2 days post-infection (Figures 1A and 1B). In contrast, mice orally pre-treated with streptomycin, a broad-spectrum antibiotic, sustain a high fecal burden of *Kpn* (Figure 1B). These results support the idea that the microbiota plays a dominant role in controlling *Kpn* colonization, making this pathogen suitable for our studies of microbiota-dependent colonization resistance.

To examine how prior infection impacts resistance to *Kpn*, we employed 2 separate mouse models: (1) the offspring of a specific-pathogen-free (SPF) mouse colony whose germ-free (GF) founders received the microbiota of wild mice (wildR model) (Rosshart et al., 2017) and (2) SPF mice previously infected with an attenuated strain (*ΔyopM*) of the food-borne pathogen *Yersinia pseudotuberculosis* (post-*ΔyopM* model) (Han et al., 2017) (Figure 1C). The first model is particularly appropriate for addressing our question since, in their natural environment, wild mice are exposed to far more infections than standard laboratory mice. We acknowledge, however, that many factors besides prior infection could also contribute to the altered microbiota of wild mice. Hence, we also turned to the more defined post-*ΔyopM* model. A key advantage of this model is that *ΔyopM* locally expands and induces gut inflammation but, unlike the *Y. pseudotuberculosis* (*Yptb*) wild-type, is completely cleared within a few days post-infection (Han et al., 2017). As such, this model allowed us to assess the impact of a transient infectious process on colonization resistance, independently of pathogen persistence.

Following oral infection, wildR mice displayed enhanced resistance to *Kpn* as compared to control SPF mice (Figure 1D). Because wildR mice were generated by transferring the microbiota of wild mice into GF mice (Figure 1C), these results support the idea that the enhanced resistance of wildR mice was primarily mediated by the microbiota. Furthermore, we also observed enhanced resistance to *Kpn* in mice previously infected with *ΔyopM* (Figure 1E). A time course of resistance to *Kpn* following *ΔyopM* infection showed that enhanced resistance is detectable only after 4 weeks post-*ΔyopM* infection and persists to at least 15 weeks post-*ΔyopM* infection (Figures 1E and S1A).

To distinguish the role of the microbiota versus host responses in *ΔyopM*-enhanced resistance, we first considered the possibility that prior infection may accelerate intestinal expulsion. However, intestinal transit time was not impacted following *ΔyopM* infection (Figure S1B). Next, we broadly surveyed both innate and adaptive immune responses in the lamina propria of the large intestines (Figures S2A–S2C), the primary site of *Kpn* colonization (Figure 1A). The most significant immune alteration that we identified was that, in mice at 4 weeks post-*ΔyopM* infection, $CD8^+$ T cells exhibit a heightened potential to produce the cytokine interferon (IFN)-γ (Figures S2C and S2D). Thus, *ΔyopM*-enhanced resistance could result from altered mucosal immune responses and/or changes to the microbiota. While both phenomena could play a role, we decided to focus our exploration on the microbiota.

To this end, we conventionalized GF mice with fecal microbiota from post-*ΔyopM* mice or control naive mice (Figure 1C). As previously reported (Han et al., 2017), we could not detect *ΔyopM* in the transferred microbiota (Figure S1C). Using this approach, we found that the microbiota from post-*ΔyopM* mice was sufficient to confer enhanced resistance to *Kpn*

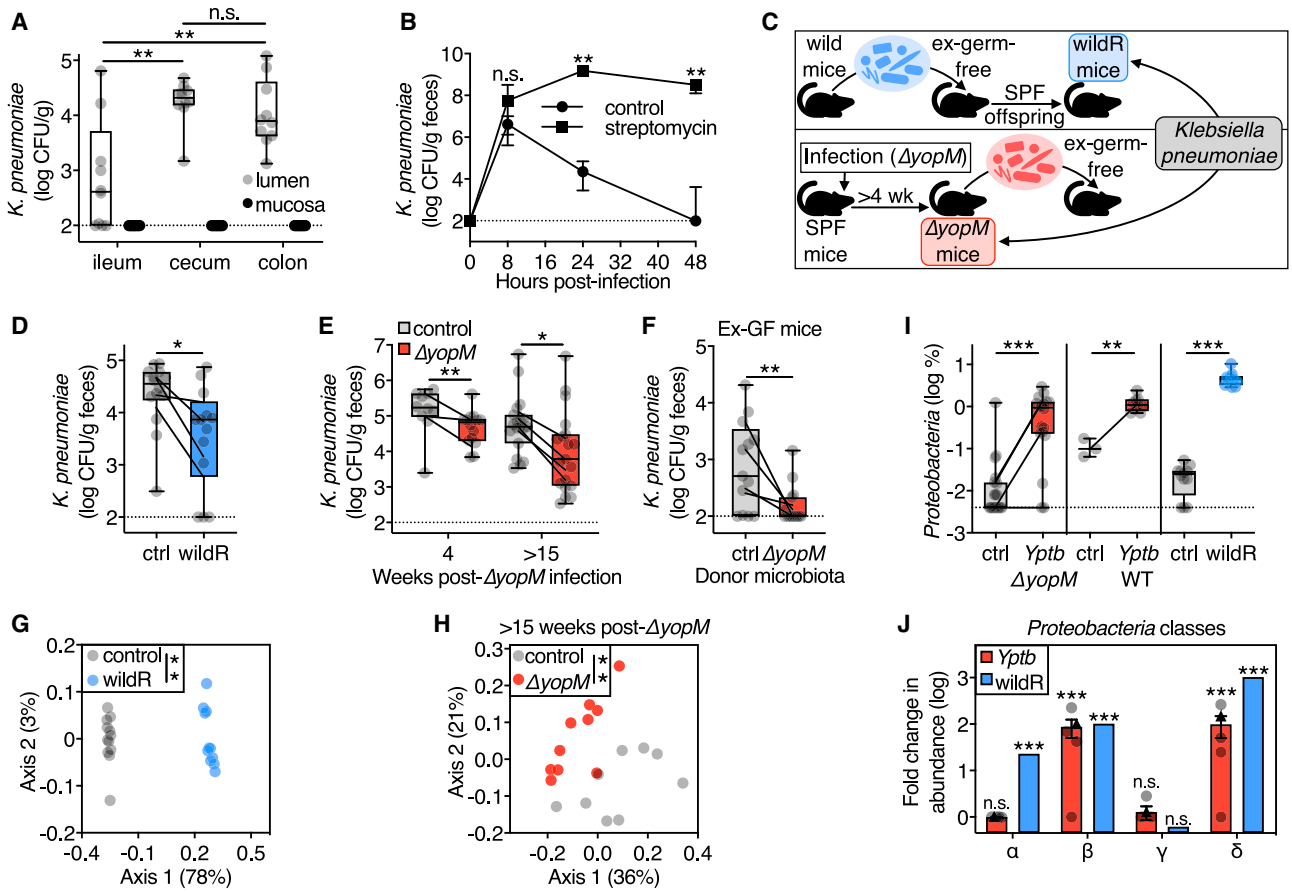

Figure 1. Infection-trained microbiota enhance colonization resistance

(A) *Kpn* colony-forming units (CFU) in the gut luminal contents and mucosal scrapings of SPF mice at 1 day (21–24 h) post-*Kpn* infection (1 experiment with 2 paired cages, n = 10).

(B) *Kpn* CFU in the feces of control (untreated) and streptomycin-treated mice. Points show median ± 95% confidence intervals (1 experiment, n = 4–5).

(C) Scheme for wildR and post-*ΔyopM* mice. For infection with *Kpn*, naive SPF mice served as the control.

(D) *Kpn* CFU in the feces of control and F10 wildR mice at 1 day post-*Kpn* infection (2 pooled experiments, n = 14, fold decrease = 14). An outlier was identified and removed using Grubbs' method with $\alpha = 0.0001$.

(E) *Kpn* CFU, at 1 day post-*Kpn* infection, in the feces of control and post-*ΔyopM* mice at 4 weeks post-*ΔyopM* infection (2 experiments, n = 10–14, fold decrease = 6) and >15 weeks post-*ΔyopM* infection (4 experiments, n = 19–20, fold decrease = 13).

(F) *Kpn* CFU in the feces of ex-GF mice, conventionalized with the microbiota of control or post-*ΔyopM* mice, at 1 day post-*Kpn* infection (2 pooled experiments, n = 13–15, fold decrease = 7).

(G and H) Principal coordinates analysis (PCoA) plots of unweighted UniFrac distances between the 16S profiles of (G) control and F2 wildR mice (n = 11–12) and (H) control and post-*ΔyopM* mice at >15 weeks post-*ΔyopM* infection (n = 9–10). Percentages represent the variance explained by each PC.

(I) Relative abundance of *Proteobacteria* in the gut microbiota of post-*Yptb ΔyopM* (4 experiments, n = 18–20, fold increase = 69), post-*Yptb* WT (1 experiment, n = 3–9, fold increase = 11), F2 wildR (3 experiments, n = 11–12, fold increase = 164), and respective control mice.

(J) Fold change in the median abundance of *Proteobacteria* classes in the gut microbiota of post-*Yptb* versus control mice (circles, *Yptb ΔyopM*; triangles, *Yptb* WT; n = 23–27) and F2 wildR versus control mice (n = 11–12). Post-*Yptb* bars show mean ± SEM of 5 paired cages.

The control for post-*Yptb* (*ΔyopM* and WT) and F10 wildR mice was naive SPF mice. The control for F2 wildR mice was F2 labR mice. In box and whisker plots, lines connect the medians of paired cages. Dotted lines indicate the detection limit. n.s., not significant; *p < 0.05; **p < 0.01; ***p < 0.001 by Mann-Whitney test (A–F and I; in J, with Benjamini-Hochberg correction) or PERMANOVA (G and H). See also Figures S1 and S2 and Table S1.

(Figure 1F). Notably, resistance resulting from microbiota transfer occurred in the absence of enhanced CD8$^+$ T cell responses (Figure S2E). These findings illustrate that a single mild infection is sufficient to remodel the microbiota in a way that enhances resistance to *Kpn*.

We next analyzed the community compositions of the post-*ΔyopM* and wildR microbiota, with the goal of identifying commonly enriched taxa that may enhance colonization resistance. Thus, we examined the 16S rRNA gene profiles of the wildR microbiota (F2 generation from a previously published study [Rosshart et al., 2017]) and the post-*ΔyopM* microbiota. Unlike the post-*ΔyopM* microbiota (which was compared to naive SPF microbiota as a control), the wildR microbiota exhibited higher alpha diversity compared to its control (microbiota

of F2 labR mice, or mice whose GF founders received the microbiota of laboratory mice [Rosshart et al., 2017]) (Figure S1D). On the other hand, both wildR and post-*ΔyopM* microbiota profiles clustered separately from their controls according to beta diversity analyses (Figures 1G and 1H), and this separation persisted to the F10 (contemporary) generation of wildR mice and was maintained after transfer of the post-*ΔyopM* microbiota into GF mice (Figures S1E and S1F).

While we did not discern consistent major shifts in highly abundant phyla (Figures S1G an S1H), a normally minor phylum, *Proteobacteria*, was the only phylum to be enriched in both the post-*ΔyopM* and wildR microbiota (both F2 and F10 generations) (Figure S1H; Table S1), expanding about 100-fold from 0.01% to 1% following infection with *ΔyopM* and in wildR mice compared to control mice (Figure 1I). Several members of the *Proteobacteria* phylum, especially those within the class *Gammaproteobacteria*, are known to expand in the context of infection and inflammation (Molloy et al., 2013). However, in our settings, the only *Proteobacteria* classes to be significantly increased in both the post-*ΔyopM* and wildR microbiota (F2 and F10), as compared to their control microbiota, were the *Deltaproteobacteria* and the *Betaproteobacteria* (Figures 1J and S1I). Furthermore, following transfer of the post-*ΔyopM* microbiota into GF mice, the only *Proteobacteria* species to remain enriched was a deltaproteobacterium (Figure S1J; Table S1). Thus, microbiota profiles associated with enhanced resistance to *Kpn* are enriched for *Deltaproteobacteria*, supporting the idea that these bacteria may promote colonization resistance.

Infection-trained microbiota are enriched for taurine-utilizing taxa

Due to the enrichment of *Proteobacteria* in both the post-*ΔyopM* and wildR microbiota, we hypothesized that they may harbor common community functions. To probe this possibility, we examined the shotgun metagenomes of the wildR (F2 generation) and post-*ΔyopM* microbiota. Relative to its control metagenome, the post-*ΔyopM* metagenome was enriched for 46 functions, while the wildR metagenome was enriched for 379 functions (Enzyme Commission numbers [McDonald et al., 2009]) (Figure 2A; Table S2). Of these enriched functions, 18 were shared (Figure 2B), and 6 of these 18 could be assigned to 2 metabolic pathways: sulfur metabolism and menaquinone biosynthesis (Figures 2C and 2D).

In agreement with the expansion of *Deltaproteobacteria* in the post-*ΔyopM* and wildR microbiota (Figure 1J), the primary source of the sulfur metabolism pathway was a deltaproteobacterium (*Desulfovibrio* genus) in the post-*ΔyopM* metagenome (blue wedges, Figure 2D) and a mixture of *Deltaproteobacteria* in the wildR metagenome (blue wedges, Figure S3A). A prevalent characteristic of *Deltaproteobacteria* is the ability to gain energy from anaerobic respiration with sulfur-containing compounds such as taurine or sulfate (Peck et al., 2019) (Figure 2E). Specifically, these bacteria first convert taurine or sulfate to sulfite via taurine-pyruvate aminotransferase (encoded by *tpa*) or sulfate adenylyltransferase (*sat*), respectively. Then, they reduce sulfite to sulfide via dissimilatory sulfite reductase (*dsr*) using electrons donated by menaquinone electron shuttles (Barton et al., 2017) (Figure 2E). To distinguish whether taurine and/or sulfate drives the *Deltaproteobacteria* expansion in the post-*ΔyopM* and wildR microbiota, we assessed the abundance of *tpa* and *sat* in their metagenomes. While *tpa* was significantly higher in both metagenomes, *sat* showed a modest increase in only the wildR metagenome, suggesting that taurine rather than sulfate contributes to the expansion of *Deltaproteobacteria* (Figure 2C).

Because metagenomics can only give insight into the microbiota's functional potential, we next set out to more directly determine whether taurine is indeed elevated in the gut following infection. To this end, we profiled the abundance of 186 defined metabolites using gas chromatography time-of-flight mass spectrometry and in total identified 13 metabolites that were more abundant in the cecal contents of post-*ΔyopM* mice than those of control mice (Figures 2F and S3B; Table S3). Five of these 13 metabolites were the substrate, precursors, or byproducts of xanthine oxidase (metabolites in bold in Figure S3B), a host antimicrobial effector known to be induced by enteric pathogens (Martin et al., 2004). Notably and confirming our metagenomics-based prediction, taurine was the most significantly increased metabolite in post-*ΔyopM* mice (Figures 2F and S3B).

In the gut, a dominant source of taurine is bile acids (Wahlström et al., 2016). These host detergents are synthesized and conjugated to taurine in the liver, stored in the gallbladder, and released into the gut to aid fat/oil digestion (Figure 2G). Once in the gut, bile acids are chemically transformed by specific members of the microbiota. These transformations include deconjugation, which releases taurine from primary (host-synthesized) bile acids, making taurine bioavailable to the entire microbiota, and dehydroxylation into secondary (microbiota-derived) bile acids (Wahlström et al., 2016) (Figure 2G). The latter activity is encoded by the *bai* operon, and a gene within this operon (*baiE*) was jointly enriched in the post-*ΔyopM* and wildR metagenomes, suggesting heightened bile-acid-directed activity in the gut microbiota of these mice (Figure 2C).

Because bile acids are synthesized in the liver, we assessed this organ for broad changes post-infection. Post-*ΔyopM* mice, however, did not exhibit gross signs of liver damage based on histology (Figures S3D and S3E). On the other hand, whole-tissue RNA sequencing (RNA-seq) of post-*ΔyopM* livers revealed differential expression of 894 genes. The 792 upregulated genes were functionally enriched for pathways (Gene Ontology terms [Ashburner et al., 2000]) related to inflammation, cytokine production, and leukocyte activity (Figure S3F; Table S4). In line with this, post-*ΔyopM* liver-derived $\gamma\delta$, $CD4^+$, and $CD8^+$ T cells exhibited heightened production of various pro-inflammatory cytokines (Figure S3G). Although these cytokines, in particular interleukin-17 (IL-17), are associated with bile-acid-induced inflammation (Li et al., 2017), only 3 genes (*Vdr*, *Slc10a6*, *Slco1a1*) mediating bile acid signaling/transport were differentially expressed in post-*ΔyopM* livers, suggesting that most *ΔyopM*-induced changes to bile acid metabolism may occur post-transcriptionally or outside the liver. Supporting this, post-*ΔyopM* mice sustained enlarged gallbladders (Figure S3H) and higher intestinal levels of total bile acids (Figure S3I). Thus, a transient infection can induce long-term heightened immunity within the liver, the organ responsible for synthesizing bile acids, along with alterations to the gallbladder, the organ responsible for storing bile acids. Of interest, wildR mice also sustained

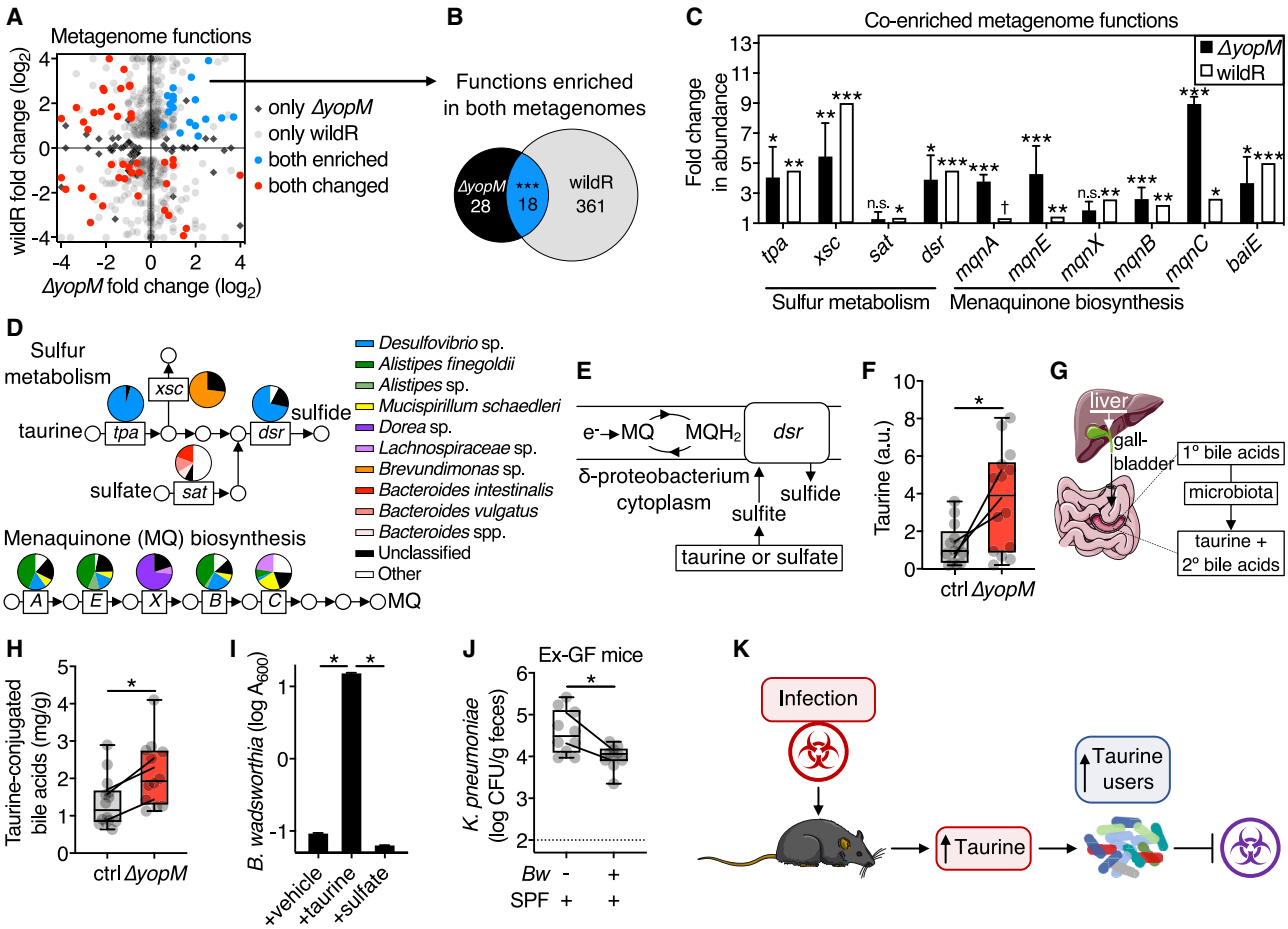

Figure 2. Infection-trained microbiota are enriched for taurine-utilizing taxa

(A) Fold changes in the median abundance of functions (EC numbers with $\log_2$ fold change > 0.5, $p < 0.05$) in the shotgun metagenome of post-*ΔyopM* mice at >15 weeks post-*ΔyopM* infection (compared to naive SPF mice) versus F2 wildR mice (compared to F2 labR mice). Functions differentially abundant in only post-*ΔyopM* mice are black diamonds; only wildR, gray circles; enriched in both post-*ΔyopM* and wildR, blue; differentially abundant in both post-*ΔyopM* and wildR, red.

(B) Number of functions co-enriched in the post-*ΔyopM* and F2 wildR metagenomes.

(C) Fold change in the median abundance of functions enriched in the metagenome of post-*ΔyopM* versus naive SPF mice (n = 11) and F2 wildR versus F2 labR mice (n = 10). Post-*ΔyopM* bars show mean ± SEM of 3 paired cages.

(D) Pathways enriched in the post-*ΔyopM* metagenome. Pie charts represent the relative contribution of taxa to a function. *A*, *mqnA* (same for *E*, *X*, *B*, and *C*); MQ, menaquinone; other, aggregate of rare taxa.

(E) Model for *Deltaproteobacteria* energy generation. MQ, oxidized menaquinone; MQH_2, reduced menaquinone.

(F) Abundance of taurine in the cecal contents of control and post-*ΔyopM* mice at >15 weeks post-*ΔyopM* infection (3 pooled experiments, n = 13–14, fold increase = 4.7). a.u., arbitrary units.

(G) The microbiota converts primary (1°) bile acids to taurine and secondary (2°) bile acids.

(H) Abundance of total taurine-conjugated bile acids in the cecal contents of control and post-*ΔyopM* mice at >15 weeks post-*ΔyopM* infection (3 pooled experiments, n = 12–14, fold increase = 1.6).

(I) Growth yield (measured by absorbance at 600 nm) of *B. wadsworthia* in rich media + vehicle, taurine, or sulfate. Bars show mean ± SEM (1 experiment, n = 4).

(J) *Kpn* CFU in the feces of ex-GF mice, conventionalized with SPF microbiota ± pre-engraftment with *B. wadsworthia* (*Bw*), at 1 day post-*Kpn* infection (2 pooled experiments, n = 10, fold decrease = 5.3). The dotted line indicates the detection limit.

(K) Model: elevated taurine post-infection enriches for gut taxa that utilize taurine.

In box and whisker plots, lines connect the medians of paired cages. n.s., not significant; *$p < 0.05$; **$p < 0.01$; ***$p < 0.01$ by Mann-Whitney (A, C, F, and H–J) or hypergeometric (B) test. See also Figure S3 and Tables S2 and S3.

higher intestinal levels of total bile acids (Figure S3J) but lower levels of taurine, a potential result of enhanced consumption by the microbiota (Figure S3C).

Because bile acids are highly heterogeneous, we next profiled the abundance of 23 defined bile acids using liquid chromatography-mass spectrometry. Total taurine-conjugated bile acids as well as individual primary and secondary bile acids were elevated in the cecal contents of post-*ΔyopM* mice (Figures 2H and S3K; Table S3). Collectively, these results propose that even a transient infectious encounter can have long-term

consequences on host bile acid metabolism, resulting in a sustained increase in intestinal taurine, a phenomenon that may lead to the expansion of taurine-utilizing *Deltaproteobacteria* (Figure 2K).

To assess whether taurine-utilizing *Deltaproteobacteria* contribute to colonization resistance, we chose the deltaproteobacterium *Bilophila wadsworthia* ATCC 49260 as a model. As predicted for the *Deltaproteobacteria* in the post-*ΔyopM* and wildR metagenomes (Figure 2C), this strain flourishes on taurine, but not sulfate (Figure 2I), in a menaquinone-dependent manner (Figure S3L). To preferentially enrich the gut microbiota with *B. wadsworthia*, we colonized GF mice with mono-cultures of *B. wadsworthia* prior to conventionalizing these mice with complex SPF microbiota. This procedure resulted in a nearly 8-fold increase in *B. wadsworthia* (Figure S3M; Table S1) and was sufficient to enhance resistance to *Kpn* (Figure 2J). Together, these results support the idea that the expansion of taurine-utilizing *Deltaproteobacteria* can directly contribute to colonization resistance (Figure 2K).

Taurine-trained microbiota enhances colonization resistance

Our results thus far support the idea that elevated taurine may by itself promote colonization resistance. To test this, we placed mice onto taurine-supplemented drinking water for 2–3 weeks prior to infection with *Kpn* (Figure 3A). Fecal measurements showed that this procedure was able to slightly increase the available taurine in the distal colon without altering total bile acids (Figure 3B). Notably, even a slight increase in colonic taurine levels was sufficient to increase resistance to *Kpn* (Figure 3C). Suggesting a role for the gut microbiota, taurine supplementation did not enhance intestinal expulsion or resistance to *Kpn* airway infection (Figures S4A–S4C).

Besides serving as a microbial nutrient, taurine has been shown to stimulate host antimicrobial defenses (Levy et al., 2015). To distinguish whether the microbiota or host primarily mediates taurine-enhanced resistance, we first assessed immune cell composition in the large intestinal lamina propria and epithelium via flow cytometry and RNA-seq, respectively. These approaches revealed that taurine alone elicits neither innate nor adaptive immune responses in the lamina propria and only modestly alters gene expression in purified epithelial cells (all $\log_2$ fold changes <0.5, Figures S4D–S4F; Table S4). Interestingly, nearly half (10/21) of the upregulated genes encoded ribosomal proteins, suggesting that taurine primarily stimulates epithelial cell growth and translation rather than antimicrobial defense. Next, we assessed whether taurine can enhance resistance to *Kpn* in mice devoid of microbiota (Figure S4G). However, taurine treatment of GF mice did not alter protection (Figure S4H). While less powered than our SPF experiments (Figure 3C), our GF experiments nevertheless suggest that, under certain settings, the microbiota may be required for taurine-enhanced resistance. To confirm this, we transferred the fecal microbiota of taurine or vehicle-treated mice into GF mice. Further supporting a role for the microbiota, the taurine-trained microbiota promoted greater resistance to *Kpn* (Figure 3D).

To determine whether taurine can enhance resistance to other pathogens, we utilized *Citrobacter rodentium*, a murine model for pathogenic *E. coli* (Figure S4I). *C. rodentium* primarily colonizes the colon, where one of its virulence strategies is to induce the hyperplasia of colonic crypts. Because epithelial colonocytes represent a major source of oxygen in the colon lumen, crypt hyperplasia promotes *C. rodentium* aerobic respiration and luminal proliferation (Lopez et al., 2016). Beginning at day 3 post-infection, taurine induced a 1 to 3 log decrease in *C. rodentium* fecal burden (Figures 3E and S4J) and was also able to mitigate crypt hyperplasia (Figures S4K and S4L). Thus, these results further demonstrate taurine's ability to enhance colonization resistance.

We next assessed the impact of taurine on gut microbial ecology. Because pathways for metabolizing taurine are taxonomically widespread (Cook and Denger, 2006), we predicted that diverse taxa would have the potential to benefit and expand in response to taurine. In line with this, 16S profiling revealed that taurine remodeling of the gut microbiota is highly variable at the taxonomic level (Figure 3F; Table S1). This remodeling, however, was conserved at the functional level, as revealed by shotgun metagenomics, where one of the largest increases was in the gene encoding dissimilatory sulfite reductase (*dsr*) (Figure 3G; Table S2). The *dsr* gene product catalyzes the final step in taurine metabolism (Figure 2E), and, consistent with taurine shaping the post-*ΔyopM* and wildR microbiota, both of their metagenomes were also enriched for *dsr* (Figure 2C). In the taurine-trained metagenome, the primary sources of *dsr* were *Clostridiales* (Figure 3H), and accordingly, many *Clostridiales* also expanded following taurine treatment (Figure 3F). Of note, these taxa were distinct from the primary source of *dsr* (*Deltaproteobacteria*) in the post-*ΔyopM* and wildR microbiota (Figures 2D and S3A). Thus, both taurine supplementation and prior infection enrich for members of the microbiota that functionally share the capacity for metabolizing taurine via *dsr*.

A major byproduct of taurine metabolism, resulting directly from *dsr* activity, is the poisonous gas hydrogen sulfide (Barton et al., 2017). Based on our metagenomics data (Figure 3G), we predicted that the taurine-trained microbiota would produce more sulfide than vehicle-treated microbiota. To test this, we utilized an *ex vivo* culture-based approach, allowing us to modulate the microbiota's growth environment. Confirming our metagenomics-based prediction, the microbiota of taurine-treated mice was highly responsive to taurine addition *ex vivo*, producing significantly more sulfide than the microbiota of vehicle-treated mice (Figure 3I). Together, these data support the idea that training of the microbiota with taurine, a bile-acid-derived metabolite that is elevated by pathogenic exposures, potentiates the microbiota's ability to produce sulfide (Figure 3J).

Taurine-derived sulfide inhibits pathogen respiration

At high concentrations, hydrogen sulfide can inhibit the activity of cytochrome oxidases, the terminal enzymes in aerobic electron transport chains (Forte et al., 2016). Because aerobic respiration is exploited by pathogens to access non-fermentable growth substrates (Lopez et al., 2016) and because taurine potentiates sulfide production by the microbiota (Figure 3I), we proposed the following model for taurine-enhanced colonization resistance: at low levels of taurine, oxygen enables pathogens

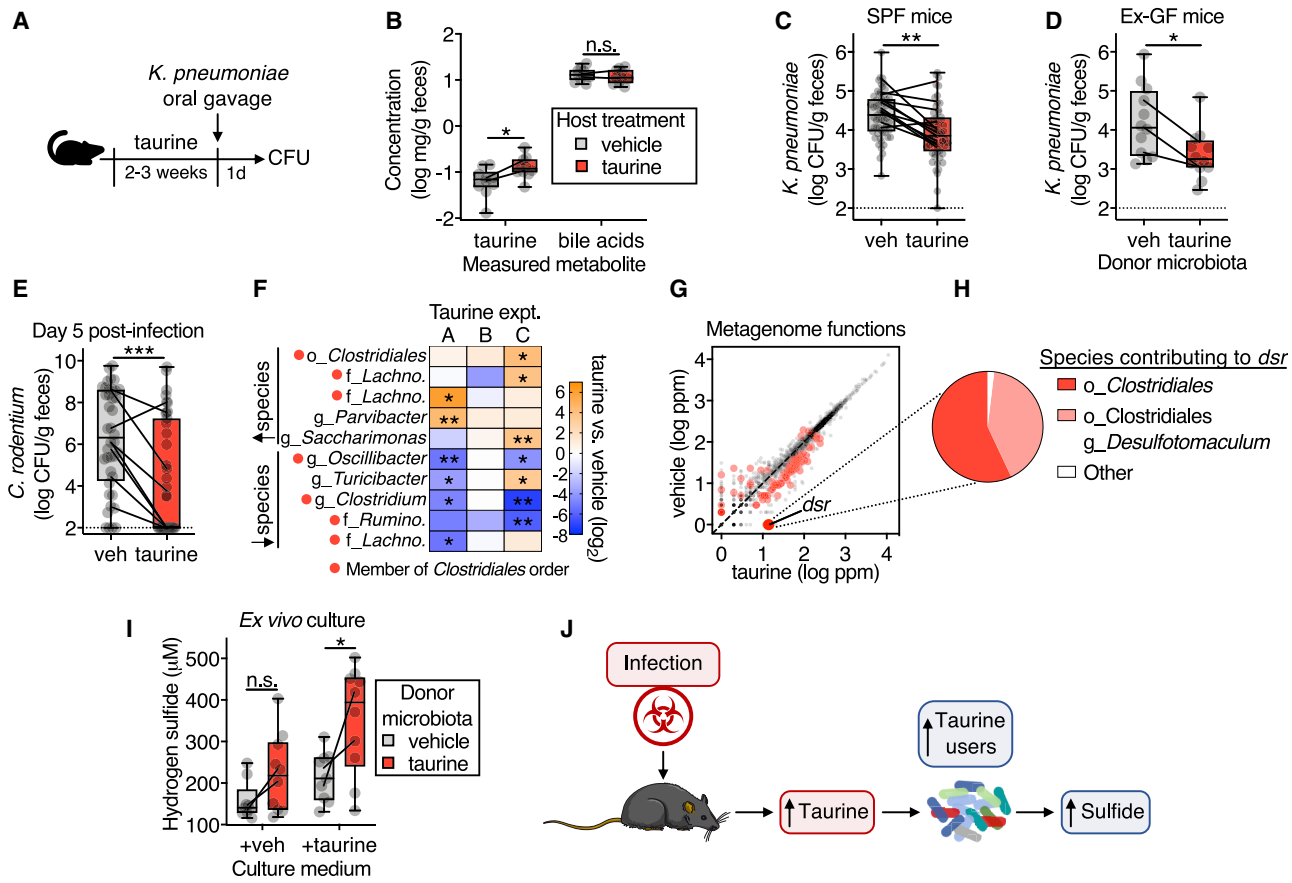

Figure 3. Taurine-trained microbiota enhances colonization resistance

(A) Scheme for taurine treatment. Mice were placed onto drinking water (vehicle) ± 200 mM taurine for 2–3 weeks prior to *Kpn* infection.

(B) Abundance of taurine and total bile acids in the feces of vehicle and taurine-treated mice (1 experiment with 2 paired cages, n = 10, taurine fold increase = 2.1).

(C) *Kpn* CFU in the feces of vehicle and taurine-treated mice at 1 day post-*Kpn* infection (8 pooled experiments, n = 58–59). Lines connect the means of paired cages (fold decrease = 4.5; for medians of paired cages, fold decrease = 2.1).

(D) *Kpn* CFU in the feces of ex-GF mice, conventionalized with the microbiota of vehicle or taurine-treated mice, at 1 day post-*Kpn* infection (2 pooled experiments, n = 12, fold decrease = 11).

(E) *C. rodentium* CFU in the feces of vehicle and taurine-treated mice at 5 days post-*C. rodentium* infection (5 pooled experiments, n = 39–40, fold decrease = 241).

(F) Ten most differentially abundant species that were significant in at least 1 of 3 paired groups of vehicle and taurine-treated mice (experiment A, B, and/or C). Species are named according to their lowest taxonomic classification. Order, o; family, f; genus, g; *Lachno.*, *Lachnospiraceae*; *Rumino.*, *Ruminococcaceae*.

(G) Median abundance of functions (EC numbers) in the shotgun metagenome of taurine versus vehicle-treated mice. Significant functions (log_2 fold change > 0.5, $p < 0.05$) are red (2 pooled experiments, n = 9). *dsr*, dissimilatory sulfite reductase (fold increase = 8.3); ppm, parts per million (read counts assigned to a function per million total read counts).

(H) Pie chart representing the relative contribution of species to *dsr*. Species are named according to their lowest taxonomic classification (order, o; genus, g).

(I) Hydrogen sulfide released by the gut microbiota of vehicle and taurine-treated mice during *ex vivo* culture ± taurine (1 experiment with 2 paired cages, n = 9–10, fold increase = 1.6). Data are representative of 2 experiments.

(J) Model: taurine enriches for gut taxa that generate sulfide.

In box and whisker plots, lines connect the medians of paired cages, unless otherwise indicated. Dotted lines in (C)–(E) indicate the detection limit. n.s., not significant; *$p < 0.05$; **$p < 0.01$; ***$p < 0.001$ by Mann-Whitney test (B–G and I). See also Figure S4 and Tables S1 and S2.

to access non-fermentable substrates, whereas at high levels of taurine (such as in post-*ΔyopM* or taurine-supplemented mice), taurine-derived sulfide restricts pathogens from these substrates (Figure 4A).

To test our model, we initially employed a high-throughput approach, transposon sequencing (Tn-seq) (Chao et al., 2016), to screen *Kpn* Tn mutants with altered fitness *in vivo*. To perform Tn-seq, we passaged an input pool of 12,000 *Kpn* Tn mutants through control and post-*ΔyopM* mice (Ramage et al., 2017). With this experimental design, if a particular gene preferentially promoted fitness in 1 of the 2 mouse groups, mutants in that gene would be preferentially depleted from that group's output pool (Figure S5A). To identify such mutants, we amplified and deep-sequenced *Kpn* genomic DNA adjacent to Tn insertions, allowing us to determine both their genomic location and abundance in the output pools. In total, we identified 125 and 79

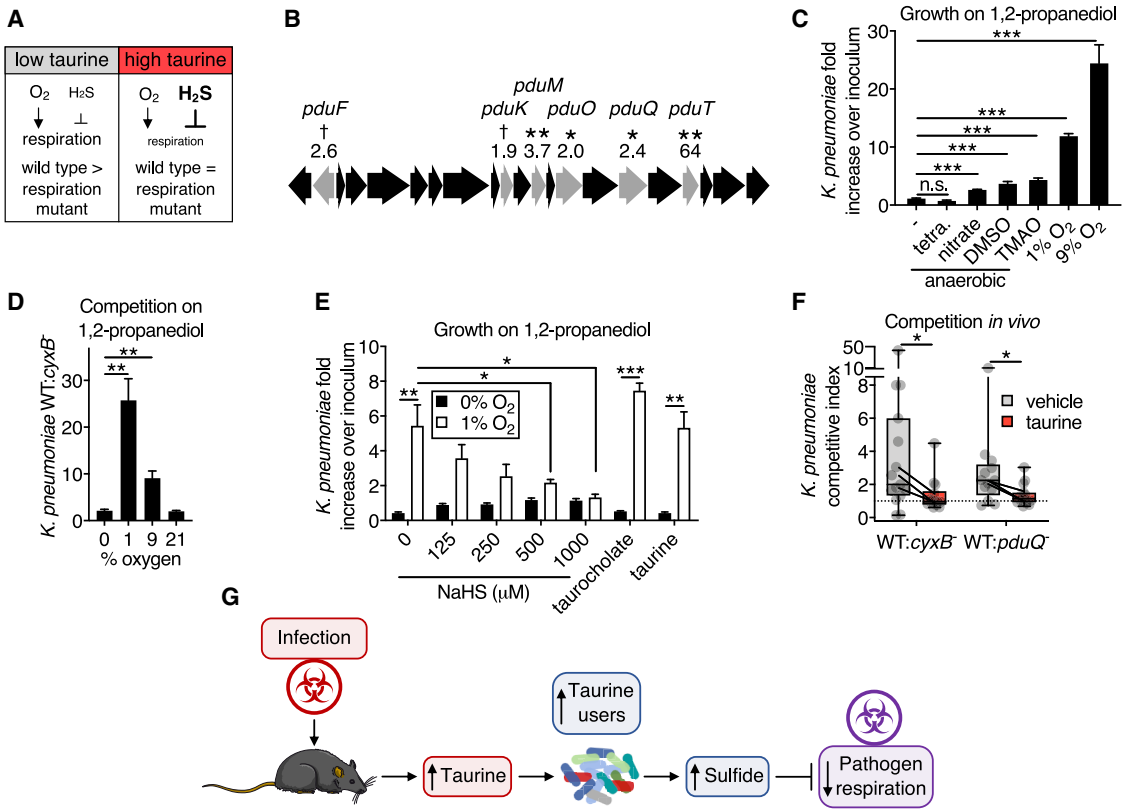

Figure 4. Taurine-derived sulfide inhibits pathogen respiration

(A) Model for taurine-enhanced colonization resistance.

(B) *Kpn* 1,2-propanediol utilization (*pdu*) gene organization. Numbers above genes in gray indicate fold decrease in control mice relative to post-*ΔyopM* mice (2 pooled experiments, n = 6–7 samples per group).

(C) Fold increase in *Kpn* CFU after growth on 1,2-propanediol (5 mM) as the sole carbon source ± an electron acceptor (50 mM). tetra., tetrathionate; DMSO, dimethyl sulfoxide; TMAO, trimethylamine N-oxide (2 pooled experiments, n = 6).

(D) The competitive index (CI, output ratio divided by input ratio of WT:mutant) of the *Kpn* WT and *cyxB*$^-$ mutant after growth on 1,2-propanediol ± oxygen (2 pooled experiments, n = 6).

(E) Fold increase in *Kpn* CFU after growth on 1,2-propanediol ± sodium hydrosulfide (NaHS), taurocholate (5 mM), or taurine (5 mM) (2 pooled experiments, n = 4).

(F) The CI of *Kpn* WT:*cyxB*$^-$ and WT:*pduQ*$^-$ in the feces of vehicle and taurine-treated mice at 1 day post-*Kpn* infection (2 pooled experiments, n = 14–15, fold decrease = 2). The dotted line indicates equal fitness between WT and mutant. Lines connect the medians of paired cages.

(G) Model: sulfide generated by the gut microbiota from taurine inhibits pathogen respiration.

Bars show mean ± SEM. n.s., not significant; †p < 0.1; *p < 0.05; **p < 0.01; ***p < 0.001 by Mann-Whitney (C–F) or Wald (B) test. See also Figure S5 and Table S5.

genes that differentially promote *Kpn* fitness in control and post-*ΔyopM* mice, respectively (Table S5).

Based on our model (Figure 4A), we first queried our Tn-seq results for *Kpn* genes that mediate anaerobic respiration. In bacteria, respiration can be performed not only with oxygen but also anaerobic electron acceptors, such as nitrate. While defined enteric pathogens have been demonstrated to exploit anaerobic respiration to colonize the gut (Faber et al., 2017), our model proposes that taurine-derived sulfide specifically inhibits aerobic respiration. Accordingly, Tn-seq confirmed the inability of genes that mediate anaerobic respiration to differentially contribute to *Kpn* fitness in either control or post-*ΔyopM* mice (Figure S5B).

We next queried our Tn-seq results for *Kpn* genes that mediate growth on non-fermentable substrates. Based on our model, we focused on substrates, such as formate (Lopez et al., 2016), that gut pathogens have been reported to exploit *in vivo* via aerobic respiration (Figure S5B). Among the genes that we examined, most striking was that 4 of the 21 genes in the 1,2-propanediol utilization (*pdu*) locus promoted *Kpn* fitness in control rather than post-*ΔyopM* mice (enrichment p = 0.003, hypergeometric test) (Figures 4B and S5B). 1,2-propanediol is a byproduct of fermentation by the microbiota, but, being strictly respiratory, it itself can only be utilized in the presence of an electron acceptor (Faber et al., 2017). While anaerobic electron acceptors could fuel *Kpn* growth on 1,2-propanediol, we found that *Kpn* grew maximally on 1,2-propanediol with oxygen (Figure 4C).

Based on this finding, we next queried our Tn-seq results for terminal oxidases that potentially support *Kpn* growth on 1,2-propanediol *in vivo*. Indeed, Tn-seq identified a putative oxidase that, like the *pdu* locus, contributed to *Kpn* fitness in control mice (Figure S5B). The gene encoding this oxidase was homologous (>68% identical in amino acid sequence) to the *cyxB*-encoded

subunit of the *Salmonella* cytochrome oxidase *bd*-II (Rivera-Chávez et al., 2016). To confirm that *Kpn cyxB* promotes 1,2-propanediol utilization, we competed the wild-type (WT) against a *cyxB*$^{-}$ mutant in minimal media with 1,2-propanediol as the sole carbon source. At the level of oxygen in air (21%), the *cyxB*$^{-}$ mutant exhibited fitness comparable to the WT (Figure 4D). On the other hand, at levels of oxygen comparable to those found in the gut (<1%) (Rivera-Chávez et al., 2016), the *Kpn* WT robustly outcompeted the mutant (Figure 4D). Collectively, these data support the idea that *Kpn* utilizes 1,2-propanediol *in vivo* by scavenging oxygen via cytochrome oxidase *bd*-II.

As a further test of our model (Figure 4A), we next assessed whether sulfide could directly block 1,2-propanediol utilization. Indeed, >250 μM sulfide potently inhibited the ability of *Kpn* to grow on 1,2-propanediol with oxygen (Figure 4E). In contrast, precursors to sulfide, the taurine-conjugated bile acid taurocholate and taurine, were not inhibitory, suggesting that conversion of these precursors to sulfide is necessary for inhibition (Figure 4E). Another prediction of our model is that under low-taurine/sulfide conditions, when respiration is possible, *Kpn* should experience a growth advantage and thus be able to outcompete a *Kpn* respiration mutant. In contrast, under high-taurine/sulfide conditions, when respiration is limited, *Kpn* should not experience a growth advantage and thus be more equal in fitness to a *Kpn* respiration mutant (Figure 4A). To test these predictions, we competed the *Kpn* WT and *cyxB*$^{-}$ respiration mutant in mice treated with the vehicle or taurine. As we predicted, in vehicle-treated mice, the WT outcompeted the respiration mutant, whereas in taurine-treated mice, the WT and mutant exhibited comparable fitness (Figures 4F and S5E). Similarly, in vehicle-treated mice, the WT outcompeted a 1,2-propanediol utilization mutant (*pduQ*$^{-}$), whereas in taurine-treated mice, the WT and mutant again exhibited comparable fitness (Figures 4F, S5C, and S5E). Further supporting our model, a *Kpn* mutant (*acrE*$^{-}$) capable of respiring with 1,2-propanediol could not be outcompeted by the WT in either vehicle or taurine-treated mice (Figures S5C–S5E).

We next tested our model in the context of *C. rodentium* infection since, like *Kpn*, *C. rodentium* exploits aerobic respiration to colonize the gut (Lopez et al., 2016). Specifically, *C. rodentium* leverages the cytochrome oxidase *bd*-I, encoded by *cydAB*, to access non-fermentable substrates such as formate (Lopez et al., 2016) (Figure S5F). As predicted, >500 μM sulfide blocks the ability of *C. rodentium* to grow on formate with oxygen (Figure S5G). Furthermore, in vehicle-treated mice, the *C. rodentium* WT ultimately outcompeted a *cydAB*$^{-}$ respiration mutant, whereas similar to our observations for *Kpn*, the competitive advantage of the WT was impeded in taurine-treated mice (Figure S5H). Together, these findings support an overarching model where taurine-driven sulfide production enhances colonization resistance, specifically by inhibiting the ability of pathogens to aerobically respire and thus access strictly respiratory substrates (Figure 4G).

Sulfide sequestration unleashes pathogen respiration

Because the microbiota produces a baseline level of sulfide (Figure 3I), we next wondered whether homeostatic sulfide itself shapes gut microbial ecology and colonization resistance. To test this, we placed mice onto drinking water containing the sulfide sequestrant bismuth subsalicylate, a compound commonly consumed in over-the-counter remedies for upset stomach (Bierer, 1990) (Figure 5A). Bismuth sequesters sulfide by forming an insoluble precipitate (Bierer, 1990), and indeed, we observed that the gut microbiota releases significantly less sulfide after bismuth treatment (Figure 5B).

This observation led us to test the following model: in the absence of bismuth, homeostatic sulfide restricts respirers from accessing oxygen, whereas in the presence of bismuth, sulfide sequestration increases oxygen availability, promoting invasion by respirers such as *Kpn* (Figure 5C). Furthermore, since respirers are endogenous to the microbiota, we predicted that sulfide sequestration would promote their expansion as well. Confirming our prediction, bismuth rapidly altered the microbiota by inducing a pronounced expansion of a *Bacilli* taxon (Figures 5D and 5E; Table S1). Isolation of this taxon revealed it to be *Enterococcus faecalis*, a frequent cause of hospital-associated infections (Centers for Disease Control and Prevention, 2019) (Figure 5F). Unlike many other *Enterococcus* species, *E. faecalis* can gain energy from aerobic respiration (Ramsey et al., 2014). In line with this, whole-genome sequencing confirmed the presence of a cytochrome oxidase (*bd*-I) in bismuth-induced *E. faecalis* (Table S5). Besides *E. faecalis*, the potentially pathogenic gammaproteobacterium *Escherichia coli* also expanded after sulfide sequestration (Figures 5E and 5F). Because *E. coli* is capable of respiring with oxygen, its co-expansion with *E. faecalis* supports our model that homeostatic sulfide shapes gut ecology by subduing low-abundance, potentially pathogenic respirers.

According to our proposed model, sulfide should restrict not only endogenous but also invading oxygen respirers (Figure 5C). To test this, we assessed the impact of sulfide sequestration on colonization resistance. As predicted by our model, we found that bismuth rendered mice highly susceptible to colonization by *Kpn*, allowing for a nearly 5 log increase in *Kpn* fecal burden (Figure 5G). Thus, our results support the idea that, by sequestering sulfide, bismuth may promote aerobic respiration by potentially pathogenic, resident members of the microbiota, and invading pathogens. A confounding factor to consider when interpreting these studies is that, in addition to sequestering sulfide, bismuth has antimicrobial properties (Bierer, 1990). Nevertheless, these results complement our overarching model that, by increasing the microbiota's production of sulfide, taurine restricts pathogen respiration and thus enhances colonization resistance (Figure 5H).

DISCUSSION

We are entering a post-antibiotics "dark age" where once curable maladies could become life threatening due to the spread of antibiotic resistance (United Nations Interagency Coordination Group on Antimicrobial Resistance, 2019). Moving forward, one possible path is to leverage the microbiota, as exemplified by fecal microbiota transplantation (Pamer, 2014). However, an obstacle to microbiota-based therapies is the microbiota's vast inter-individual heterogeneity (Suez and Elinav, 2017). As the majority of beneficial host-microbe interactions are mediated by widely conserved metabolites, therapeutically co-opting metabolites, rather than their

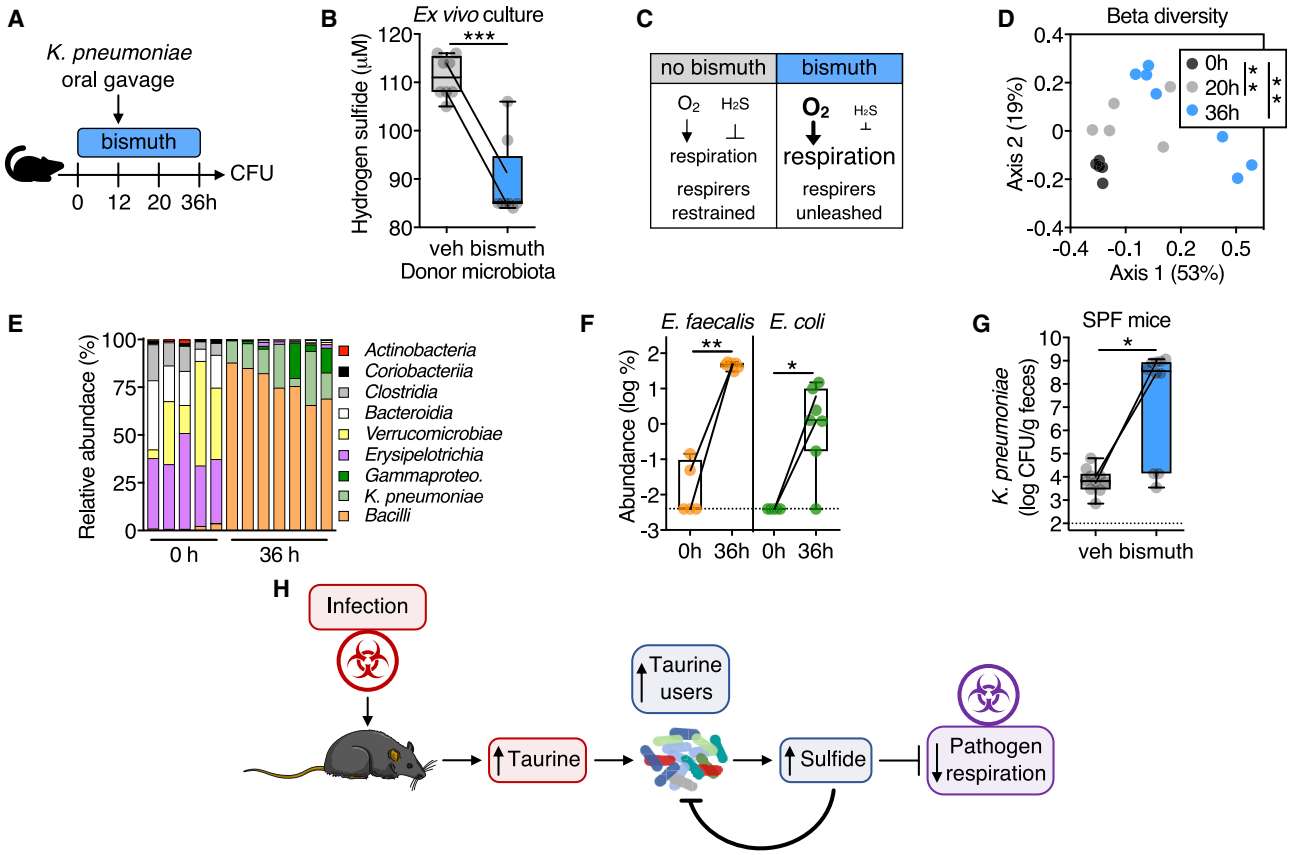

Figure 5. Sulfide sequestration unleashes pathogen respiration

(A) Scheme for bismuth treatment. Mice were placed onto drinking water (vehicle) ± 20 mM bismuth subsalicylate for 12 h prior to *Kpn* infection.

(B) Hydrogen sulfide released by the gut microbiota of vehicle and bismuth-treated mice during *ex vivo* culture (1 experiment with 2 paired cages, n = 8, fold decrease = 1.3).

(C) Model for the impact of sulfide on gut ecology.

(D) PCoA plot of unweighted UniFrac distances between the 16S profiles of mice at 0, 20, and 36 h post-bismuth treatment (1 experiment with 2 paired cages, n = 5–7). Percentages represent the variance explained by each PC.

(E and F) Relative abundance of (E) taxonomic classes and *Kpn* and (F) *E. faecalis* (*Bacilli*) and *E. coli* (*Gammaproteobacteria*) in the gut microbiota of mice at 0 and 36 h post-bismuth treatment (1 experiment with 2 paired cages, n = 5–7).

(G) *Kpn* CFU in the feces of vehicle and bismuth-treated mice at 24 h post-*Kpn* infection. Data are representative of 3 experiments. The dotted line indicates the detection limit.

(H) Model: infectious exposures increase the availability of taurine, which the gut microbiota converts to sulfide, serving to inhibit pathogen respiration and regulate the microbiota.

In box and whisker plots, lines connect the medians of paired cages. *p < 0.05; **p < 0.01; ***p < 0.001 by Mann-Whitney test (B, F, and G) or PERMANOVA (D). See also Table S5.

microbial targets/producers, may result in wider success (Suez and Elinav, 2017).

In the present work, we discovered that transient infection establishes long-term "metaorganism memory." Unlike traditional immunological memory, metaorganism memory hinges upon interdependent host and microbiota functions. Following infection, the host amplifies its production/transport of bile acids, and, in turn, the microbiota converts a bile-acid-derived metabolite, taurine, to the antimicrobial sulfide. Thus, only together do these functions bolster metaorganism resistance to subsequent infection. Because the microbiota function, the metabolism of taurine, is widely distributed (Cook and Denger, 2006), it overcomes the obstacle of inter-individual heterogeneity in microbiota composition. Furthermore, the target of sulfide, aerobic respiration, is a widely (though not universally [Neumann-Schaal et al., 2019]) distributed virulence factor.

While our work focused on how infection-elicited taurine functionally remodels the microbiota, our findings do not fully exclude a role for the immune system. Indeed, the cellular transport of taurine is critical for the establishment of immunological memory (Kaesler et al., 2012), and, besides taurine, our data suggest gut infection also elicits the innate immune effector xanthine oxidase (Martin et al., 2004) and the microbial metabolite menaquinone, a precursor of which induces antimicrobial peptides (Fukumoto et al., 2014). Thus, the immune system may work in concert with the microbiota to promote colonization resistance following infection.

Our work suggests that bile-acid-derived taurine is beneficial for colonization resistance, but, if truly the case, it raises the question of why bile acids are not always maintained at high levels. The most likely answer is that excessive bile acids are associated with various inflammatory disorders and cancers (Jia et al., 2018). Despite this, bile acids are upregulated by enteric infections, most likely because they are antimicrobial and aid pathogen clearance (Uribe et al., 2016). An outstanding question is what infection-induced signaling events lead to host upregulation of bile acids. While this question is made particularly challenging by the numerous receptors and pathways that control bile acid metabolism (Jia et al., 2018), potential candidates are the farnesoid X receptor and the hormone fibroblast growth factor 15 (Romain et al., 2013; Uribe et al., 2016).

Together, our work highlights the key contribution of taurine and sulfide to the trainable resistance of the gut microbiota to infection. By probing the consequence of pathogenic exposures on colonization resistance, we discovered that host metaorganisms adapt to infections by nourishing their gut microbiota with taurine, a strategy that serves to boost the microbiota's production of sulfide and ensure its heightened resistance against future pathogen invasions.

STAR★METHODS

Detailed methods are provided in the online version of this paper and include the following:

- KEY RESOURCES TABLE
- RESOURCE AVAILABILITY
  - Lead contact
  - Materials availability
  - Data and code availability
- EXPERIMENTAL MODEL AND SUBJECT DETAILS
  - Mice
  - Bacteria
- METHOD DETAILS
  - Intestinal infection of mice with gut pathogens
  - Treatment of mice with taurine, bismuth, and streptomycin
  - Collection and processing of gut samples to determine CFU
  - Determination of CFU
  - Preparation of NCE medium
  - Kpn and C. rodentium *in vitro* growth assays
  - B. wadsworthia *in vitro* growth assays
  - Construction of C. rodentium cydAB mutant
  - Lung infection of mice with Kpn
  - Preservation of microbiota
  - Conventionalization of GF mice
  - 16S rRNA gene profiling
  - Shotgun metagenomics
  - Profiling of metabolites by mass spectrometry
  - Measurement of fecal taurine and total bile acids
  - Measurement of sulfide production by *ex vivo* microbiota cultures
  - Tn-seq
  - Processing of large intestines and livers for flow cytometry
  - Flow cytometry
  - Processing of large intestines for epithelial cell sorting
  - Liver and gut epithelial cell RNA-seq
  - Measurement of gallbladder weight
  - Liver and colon histology
  - Measurement of intestinal transit time
  - E. faecalis isolation, identification, and whole-genome sequencing
- QUANTIFICATION AND STATISTICAL ANALYSIS

SUPPLEMENTAL INFORMATION

Supplemental Information can be found online at https://doi.org/10.1016/j.cell.2020.12.011.

ACKNOWLEDGMENTS

This work was supported by the Intramural Research Programs of NIAID (1ZIAAI001115-11 to Y.B.), NIDDK (1ZIADK054508-22 to B.R.), NCI Center for Cancer Research (1ZIABC011153-11 to G.T.), and NHGRI (1ZIAHG000180-19 to J.A.S.), the NIH Director's Challenge Innovation Award Program (Y.B. and B.R.), the DDIR (Y.B. and B.R.), the NIGMS Postdoctoral Research Associate Training (PRAT) Program (1FI2GM128736-01 to A.S.), the NIH (A.S.), the Pew Latin American Fellows Program (V.A.-O.), the Deutsche Forschungsgemeinschaft (HI 2088/1-1 to B.H.), the Human Frontier Science Program (LT000191/2018 to A.I.L.), and the Cancer Research Institute Irvington Postdoctoral Fellowship Program (M.E.). We thank Xingyao He, Shreni Mistry, and Naisarg Modi (NIAID Microbiome Program); Nicolas Bouladoux, Ejae Lewis, and Dana Trageser-Cesler (NIAID Microbiome Program Gnotobiotic Animal Facility); Kelly Paglia (West Coast Metabolomics Center); Shurjo Sen (NCI Cancer and Inflammation Program); Galina Koroleva (NIH Center for Human Immunology); Kim Webber (Belkaid laboratory), Mirian Krystel De Siqueira (now UCLA), and Austin Hall (now UW-Madison) for technical assistance;Margery Smelkinson (NIAID Biological Imaging Section) for imaging tissue sections; Michael Eckhaus (NIH Division of Veterinary Resources) for scoring liver sections; Krystyna Szymczyk (NIAID Research Technologies Branch) for assisting with *E. faecalis* identification; Gad Frankel (Imperial College London) for providing *C. rodentium* ICC169; Andreas Bäumler (UC Davis) for providing pCAL60; the NIAID and NIDDK animal facilities; the NIH HPC Biowulf cluster (https://hpc.nih.gov/); and Les Laboratoires Servier (https://smart.servier.com/). We also thank Ivan Vujkovic-Cvijin and other members of the Belkaid laboratory for providing additional expertise and support.

AUTHOR CONTRIBUTIONS

A.S. and Y.B. designed the study and wrote the manuscript; A.S. performed experiments, analyzed 16S and Tn-seq data, and interpreted results; V.A.-O. helped to initiate the study and generated Tn-seq libraries; B.H., J.H.O., and B.R. assisted with wildR mice; J.A.M. and G.T. analyzed shotgun metagenomics and whole-genome-sequencing data; C.K.S. and J.A.S. assisted with the *Kpn* Tn mutant library; P.J.P.-C. assisted with microbiology experiments; A.I.L. sorted gut epithelial cells; V.M.L analyzed RNA-seq data; and M.E. performed lung infections.

DECLARATION OF INTERESTS

NIDDK licensed wildR mice to Taconic Biosciences.

Received: April 30, 2020
Revised: November 19, 2020
Accepted: December 8, 2020
Published: January 15, 2021

REFERENCES

Ashburner, M., Ball, C.A., Blake, J.A., Botstein, D., Butler, H., Cherry, J.M., Davis, A.P., Dolinski, K., Dwight, S.S., Eppig, J.T., et al.; The Gene Ontology Consortium (2000). Gene ontology: tool for the unification of biology. Nat. Genet. *25*, 25–29.

Bankevich, A., Nurk, S., Antipov, D., Gurevich, A.A., Dvorkin, M., Kulikov, A.S., Lesin, V.M., Nikolenko, S.I., Pham, S., Prjibelski, A.D., et al. (2012). SPAdes: a new genome assembly algorithm and its applications to single-cell sequencing. J. Comput. Biol. *19*, 455–477.

Barton, L.L., Ritz, N.L., Fauque, G.D., and Lin, H.C. (2017). Sulfur cycling and the intestinal microbiome. Dig. Dis. Sci. *62*, 2241–2257.

Beura, L.K., Hamilton, S.E., Bi, K., Schenkel, J.M., Odumade, O.A., Casey, K.A., Thompson, E.A., Fraser, K.A., Rosato, P.C., Filali-Mouhim, A., et al. (2016). Normalizing the environment recapitulates adult human immune traits in laboratory mice. Nature *532*, 512–516.

Bierer, D.W. (1990). Bismuth subsalicylate: history, chemistry, and safety. Rev. Infect. Dis. *12* (*Suppl 1*), S3–S8.

Bolger, A.M., Lohse, M., and Usadel, B. (2014). Trimmomatic: a flexible trimmer for Illumina sequence data. Bioinformatics *30*, 2114–2120.

Bolyen, E., Rideout, J.R., Dillon, M.R., Bokulich, N.A., Abnet, C.C., Al-Ghalith, G.A., Alexander, H., Alm, E.J., Arumugam, M., Asnicar, F., et al. (2019). Reproducible, interactive, scalable and extensible microbiome data science using QIIME 2. Nat. Biotechnol. *37*, 852–857.

Broberg, C.A., Wu, W., Cavalcoli, J.D., Miller, V.L., and Bachman, M.A. (2014). Complete Genome Sequence of Klebsiella pneumoniae Strain ATCC 43816 KPPR1, a Rifampin-Resistant Mutant Commonly Used in Animal, Genetic, and Molecular Biology Studies. Genome Announc. *2*, e00924, e14.

Bult, C.J., Blake, J.A., Smith, C.L., Kadin, J.A., and Richardson, J.E.; Mouse Genome Database Group (2019). Mouse Genome Database (MGD) 2019. Nucleic Acids Res. *47* (D1), D801–D806.

Caporaso, J.G., Lauber, C.L., Walters, W.A., Berg-Lyons, D., Huntley, J., Fierer, N., Owens, S.M., Betley, J., Fraser, L., Bauer, M., et al. (2012). Ultra-high-throughput microbial community analysis on the Illumina HiSeq and MiSeq platforms. ISME J. *6*, 1621–1624.

Centers for Disease Control and Prevention (2019). Antibiotic Resistance Threats in the United States, 2019.

Chao, M.C., Abel, S., Davis, B.M., and Waldor, M.K. (2016). The design and analysis of transposon insertion sequencing experiments. Nat. Rev. Microbiol. *14*, 119–128.

Conlan, S., Park, M., Deming, C., Thomas, P.J., Young, A.C., Coleman, H., Sison, C., Weingarten, R.A., Lau, A.F., Dekker, J.P., et al.; NISC Comparative Sequencing Program (2016). Plasmid dynamics in KPC-positive Klebsiella pneumoniae during long-term patient colonization. MBio *7*, e00742, e16.

Cook, A.M., and Denger, K. (2006). Metabolism of taurine in microorganisms: A primer in molecular biodiversity? In Taurine 6, Advances in Experimental Medicine and Biology, *Volume 583*, S.S. Oja and P. Saransaari, eds. (Boston, MA: Springer), pp. 3–13.

Dey, N., Wagner, V.E., Blanton, L.V., Cheng, J., Fontana, L., Haque, R., Ahmed, T., and Gordon, J.I. (2015). Regulators of gut motility revealed by a gnotobiotic model of diet-microbiome interactions related to travel. Cell *163*, 95–107.

Dobin, A., Davis, C.A., Schlesinger, F., Drenkow, J., Zaleski, C., Jha, S., Batut, P., Chaisson, M., and Gingeras, T.R. (2013). STAR: ultrafast universal RNA-seq aligner. Bioinformatics *29*, 15–21.

Faber, F., Thiennimitr, P., Spiga, L., Byndloss, M.X., Litvak, Y., Lawhon, S., Andrews-Polymenis, H.L., Winter, S.E., and Bäumler, A.J. (2017). Respiration of microbiota-derived 1,2-propanediol drives Salmonella expansion during colitis. PLoS Pathog. *13*, e1006129.

Fonseca, D.M., Hand, T.W., Han, S.J., Gerner, M.Y., Glatman Zaretsky, A., Byrd, A.L., Harrison, O.J., Ortiz, A.M., Quinones, M., Trinchieri, G., et al. (2015). Microbiota-dependent sequelae of acute infection compromise tissue-specific immunity. Cell *163*, 354–366.

Forte, E., Borisov, V.B., Falabella, M., Colaço, H.G., Tinajero-Trejo, M., Poole, R.K., Vicente, J.B., Sarti, P., and Giuffrè, A. (2016). The terminal oxidase cytochrome bd promotes sulfide-resistant bacterial respiration and growth. Sci. Rep. *6*, 23788.

Fukumoto, S., Toshimitsu, T., Matsuoka, S., Maruyama, A., Oh-Oka, K., Takamura, T., Nakamura, Y., Ishimaru, K., Fujii-Kuriyama, Y., Ikegami, S., et al. (2014). Identification of a probiotic bacteria-derived activator of the aryl hydrocarbon receptor that inhibits colitis. Immunol. Cell Biol. *92*, 460–465.

Goodman, A.L., Wu, M., and Gordon, J.I. (2011). Identifying microbial fitness determinants by insertion sequencing using genome-wide transposon mutant libraries. Nat. Protoc. *6*, 1969–1980.

Gorrie, C.L., Mirčeta, M., Wick, R.R., Edwards, D.J., Thomson, N.R., Strugnell, R.A., Pratt, N.F., Garlick, J.S., Watson, K.M., Pilcher, D.V., et al. (2017). Gastrointestinal carriage is a major reservoir of Klebsiella pneumoniae infection in intensive care patients. Clin. Infect. Dis. *65*, 208–215.

Goryshin, I.Y., Miller, J.A., Kil, Y.V., Lanzov, V.A., and Reznikoff, W.S. (1998). Tn5/IS50 target recognition. Proc. Natl. Acad. Sci. USA *95*, 10716–10721.

Han, S.J., Glatman Zaretsky, A., Andrade-Oliveira, V., Collins, N., Dzutsev, A., Shaik, J., Morais da Fonseca, D., Harrison, O.J., Tamoutounour, S., Byrd, A.L., et al. (2017). White adipose tissue is a reservoir for memory T cells and promotes protective memory responses to infection. Immunity *47*, 1154–1168.e6.

Heinz, S., Benner, C., Spann, N., Bertolino, E., Lin, Y.C., Laslo, P., Cheng, J.X., Murre, C., Singh, H., and Glass, C.K. (2010). Simple combinations of lineage-determining transcription factors prime cis-regulatory elements required for macrophage and B cell identities. Mol. Cell *38*, 576–589.

Hung, C.-S., Dodson, K.W., and Hultgren, S.J. (2009). A murine model of urinary tract infection. Nat. Protoc. *4*, 1230–1243.

Jia, W., Xie, G., and Jia, W. (2018). Bile acid-microbiota crosstalk in gastrointestinal inflammation and carcinogenesis. Nat. Rev. Gastroenterol. Hepatol. *15*, 111–128.

Kaesler, S., Sobiesiak, M., Kneilling, M., Volz, T., Kempf, W.E., Lang, P.A., Lang, K.S., Wieder, T., Heller-Stilb, B., Warskulat, U., et al. (2012). Effective T-cell recall responses require the taurine transporter Taut. Eur. J. Immunol. *42*, 831–841.

Kamdar, K., Khakpour, S., Chen, J., Leone, V., Brulc, J., Mangatu, T., Antonopoulos, D.A., Chang, E.B., Kahn, S.A., Kirschner, B.S., et al. (2016). Genetic and Metabolic Signals during Acute Enteric Bacterial Infection Alter the Microbiota and Drive Progression to Chronic Inflammatory Disease. Cell Host Microbe *19*, 21–31.

Kim, S., Covington, A., and Pamer, E.G. (2017). The intestinal microbiota: Antibiotics, colonization resistance, and enteric pathogens. Immunol. Rev. *279*, 90–105.

Langmead, B., and Salzberg, S.L. (2012). Fast gapped-read alignment with Bowtie 2. Nat. Methods *9*, 357–359.

Levy, M., Thaiss, C.A., Zeevi, D., Dohnalová, L., Zilberman-Schapira, G., Mahdi, J.A., David, E., Savidor, A., Korem, T., Herzig, Y., et al. (2015). Microbiota-Modulated Metabolites Shape the Intestinal Microenvironment by Regulating NLRP6 Inflammasome Signaling. Cell *163*, 1428–1443.

Li, D., Liu, C.M., Luo, R., Sadakane, K., and Lam, T.W. (2015). MEGAHIT: an ultra-fast single-node solution for large and complex metagenomics assembly via succinct de Bruijn graph. Bioinformatics *31*, 1674–1676.

Li, M., Cai, S.-Y., and Boyer, J.L. (2017). Mechanisms of bile acid mediated inflammation in the liver. Mol. Aspects Med. *56*, 45–53.

Liao, Y., Smyth, G.K., and Shi, W. (2019). The R package Rsubread is easier, faster, cheaper and better for alignment and quantification of RNA sequencing reads. Nucleic Acids Res. *47*, e47.

Lopez, C.A., Miller, B.M., Rivera-Chávez, F., Velazquez, E.M., Byndloss, M.X., Chávez-Arroyo, A., Lokken, K.L., Tsolis, R.M., Winter, S.E., and Bäumler, A.J. (2016). Virulence factors enhance Citrobacter rodentium expansion through aerobic respiration. Science *353*, 1249–1253.

Love, M.I., Huber, W., and Anders, S. (2014). Moderated estimation of fold change and dispersion for RNA-seq data with DESeq2. Genome Biol. *15*, 550.

Macpherson, A.J., de Agüero, M.G., and Ganal-Vonarburg, S.C. (2017). How nutrition and the maternal microbiota shape the neonatal immune system. Nat. Rev. Immunol. *17*, 508–517.

Martin, M. (2011). Cutadapt removes adapter sequences from high-throughput sequencing reads. EMBnet. J. *17*, 10–12.

Martin, H.M., Hancock, J.T., Salisbury, V., and Harrison, R. (2004). Role of xanthine oxidoreductase as an antimicrobial agent. Infect. Immun. *72*, 4933–4939.

McDonald, A.G., Boyce, S., and Tipton, K.F. (2009). ExplorEnz: the primary source of the IUBMB enzyme list. Nucleic Acids Res. *37*, D593–D597.

McLoughlin, K., Schluter, J., Rakoff-Nahoum, S., Smith, A.L., and Foster, K.R. (2016). Host Selection of Microbiota via Differential Adhesion. Cell Host Microbe *19*, 550–559.

Molloy, M.J., Grainger, J.R., Bouladoux, N., Hand, T.W., Koo, L.Y., Naik, S., Quinones, M., Dzutsev, A.K., Gao, J.L., Trinchieri, G., et al. (2013). Intraluminal containment of commensal outgrowth in the gut during infection-induced dysbiosis. Cell Host Microbe *14*, 318–328.

Moriya, Y., Itoh, M., Okuda, S., Yoshizawa, A.C., and Kanehisa, M. (2007). KAAS: an automatic genome annotation and pathway reconstruction server. Nucleic Acids Res. *35*, W182-5.

Netea, M.G., Domínguez-Andrés, J., Barreiro, L.B., Chavakis, T., Divangahi, M., Fuchs, E., Joosten, L.A.B., van der Meer, J.W.M., Mhlanga, M.M., Mulder, W.J.M., et al. (2020). Defining trained immunity and its role in health and disease. Nat. Rev. Immunol. *20*, 375–388.

Neumann-Schaal, M., Jahn, D., and Schmidt-Hohagen, K. (2019). Metabolism the difficile way: The key to the success of the pathogen Clostridioides difficile. Front. Microbiol. *10*, 219.

Pamer, E.G. (2014). Fecal microbiota transplantation: effectiveness, complexities, and lingering concerns. Mucosal Immunol. *7*, 210–214.

Peck, S.C., Denger, K., Burrichter, A., Irwin, S.M., Balskus, E.P., and Schleheck, D. (2019). A glycyl radical enzyme enables hydrogen sulfide production by the human intestinal bacterium *Bilophila wadsworthia*. Proc. Natl. Acad. Sci. USA *116*, 3171–3176.

Ramage, B., Erolin, R., Held, K., Gasper, J., Weiss, E., Brittnacher, M., Gallagher, L., and Manoil, C. (2017). Comprehensive arrayed transposon mutant library of Klebsiella pneumoniae outbreak strain KPNIH1. J. Bacteriol. *199*, e00352, e17.

Ramanan, D., Bowcutt, R., Lee, S.C., Tang, M.S., Kurtz, Z.D., Ding, Y., Honda, K., Gause, W.C., Blaser, M.J., Bonneau, R.A., et al. (2016). Helminth infection promotes colonization resistance via type 2 immunity. Science *352*, 608–612.

Ramsey, M., Hartke, A., and Huycke, M. (2014). The Physiology and Metabolism of Enterococci. In Enterococci: From Commensals to Leading Causes of Drug Resistant Infection, M.S. Gilmore, ed. (Boston, MA: Massachusetts Eye and Ear Infirmary).

Reese, T.A., Bi, K., Kambal, A., Filali-Mouhim, A., Beura, L.K., Bürger, M.C., Pulendran, B., Sekaly, R.P., Jameson, S.C., Masopust, D., et al. (2016). Sequential Infection with Common Pathogens Promotes Human-like Immune Gene Expression and Altered Vaccine Response. Cell Host Microbe *19*, 713–719.

Rivera-Chávez, F., Zhang, L.F., Faber, F., Lopez, C.A., Byndloss, M.X., Olsan, E.E., Xu, G., Velazquez, E.M., Lebrilla, C.B., Winter, S.E., and Bäumler, A.J. (2016). Depletion of Butyrate-Producing Clostridia from the Gut Microbiota Drives an Aerobic Luminal Expansion of Salmonella. Cell Host Microbe *19*, 443–454.

Romain, G., Tremblay, S., Arena, E.T., Antunes, L.C.M., Covey, S., Chow, M.T., Finlay, B.B., and Menendez, A. (2013). Enterohepatic bacterial infections dysregulate the FGF15-FGFR4 endocrine axis. BMC Microbiol. *13*, 238.

Rosshart, S.P., Vassallo, B.G., Angeletti, D., Hutchinson, D.S., Morgan, A.P., Takeda, K., Hickman, H.D., McCulloch, J.A., Badger, J.H., Ajami, N.J., et al. (2017). Wild Mouse Gut Microbiota Promotes Host Fitness and Improves Disease Resistance. Cell *171*, 1015–1028.e13.

Rosshart, S.P., Herz, J., Vassallo, B.G., Hunter, A., Wall, M.K., Badger, J.H., McCulloch, J.A., Anastasakis, D.G., Sarshad, A.A., Leonardi, I., et al. (2019). Laboratory mice born to wild mice have natural microbiota and model human immune responses. Science *365*, eaaw4361.

Roubaud-Baudron, C., Ruiz, V.E., Swan, A.M., Jr., Vallance, B.A., Ozkul, C., Pei, Z., Li, J., Battaglia, T.W., Perez-Perez, G.I., and Blaser, M.J. (2019). Long-term effects of early-life antibiotic exposure on resistance to subsequent bacterial infection. MBio *10*, e02820, e19.

Schindelin, J., Arganda-Carreras, I., Frise, E., Kaynig, V., Longair, M., Pietzsch, T., Preibisch, S., Rueden, C., Saalfeld, S., Schmid, B., et al. (2012). Fiji: an open-source platform for biological-image analysis. Nat. Methods *9*, 676–682.

Seemann, T. (2014). Prokka: rapid prokaryotic genome annotation. Bioinformatics *30*, 2068–2069.

Singer, J.R., Blosser, E.G., Zindl, C.L., Silberger, D.J., Conlan, S., Laufer, V.A., DiToro, D., Deming, C., Kumar, R., Morrow, C.D., et al. (2019). Preventing dysbiosis of the neonatal mouse intestinal microbiome protects against late-onset sepsis. Nat. Med. *25*, 1772–1782.

Sonnenburg, E.D., and Sonnenburg, J.L. (2019). The ancestral and industrialized gut microbiota and implications for human health. Nat. Rev. Microbiol. *17*, 383–390.

Stacy, A., Fleming, D., Lamont, R.J., Rumbaugh, K.P., and Whiteley, M. (2016). A commensal bacterium promotes virulence of an opportunistic pathogen via cross-respiration. MBio *7*, e00782, e16.

Stewart, C.J., Ajami, N.J., O'Brien, J.L., Hutchinson, D.S., Smith, D.P., Wong, M.C., Ross, M.C., Lloyd, R.E., Doddapaneni, H., Metcalf, G.A., et al. (2018). Temporal development of the gut microbiome in early childhood from the TEDDY study. Nature *562*, 583–588.

Suez, J., and Elinav, E. (2017). The path towards microbiome-based metabolite treatment. Nat. Microbiol. *2*, 17075.

United Nations Interagency Coordination Group on Antimicrobial Resistance (2019). No Time to Wait: Securing the future from drug-resistant infections. https://www.who.int/antimicrobial-resistance/interagency-coordination-group/final-report/en/.

Uribe, J.H., Collado-Romero, M., Zaldívar-López, S., Arce, C., Bautista, R., Carvajal, A., Cirera, S., Claros, M.G., and Garrido, J.J. (2016). Transcriptional analysis of porcine intestinal mucosa infected with Salmonella Typhimurium revealed a massive inflammatory response and disruption of bile acid absorption in ileum. Vet. Res. (Faisalabad) *47*, 11.

Wahlström, A., Sayin, S.I., Marschall, H.U., and Bäckhed, F. (2016). Intestinal Crosstalk between Bile Acids and Microbiota and Its Impact on Host Metabolism. Cell Metab. *24*, 41–50.

Wood, D.E., Lu, J., and Langmead, B. (2019). Improved metagenomic analysis with Kraken 2. Genome Biol. *20*, 257.

Wotzka, S.Y., Kreuzer, M., Maier, L., Arnoldini, M., Nguyen, B.D., Brachmann, A.O., Berthold, D.L., Zünd, M., Hausmann, A., Bakkeren, E., et al. (2019). Escherichia coli limits Salmonella Typhimurium infections after diet shifts and fat-mediated microbiota perturbation in mice. Nat. Microbiol. *4*, 2164–2174.

Yilmaz, P., Parfrey, L.W., Yarza, P., Gerken, J., Pruesse, E., Quast, C., Schweer, T., Peplies, J., Ludwig, W., and Glöckner, F.O. (2014). The SILVA and "All-species Living Tree Project (LTP)" taxonomic frameworks. Nucleic Acids Res. *42*, D643–D648.

Zhou, Y., Zhou, B., Pache, L., Chang, M., Khodabakhshi, A.H., Tanaseichuk, O., Benner, C., and Chanda, S.K. (2019). Metascape provides a biologist-oriented resource for the analysis of systems-level datasets. Nat. Commun. *10*, 1523.

STAR★METHODS

KEY RESOURCES TABLE

REAGENT or RESOURCE	SOURCE	IDENTIFIER
Antibodies		
Myeloid cells: anti-mouse CD45 (30-F11), BV510	BioLegend	Cat#103138; RRID:AB_2563061
Myeloid cells: anti-mouse TCRβ (H57-597), PE-CF594	BD	Cat#562841; RRID:AB_2737831
Myeloid cells: anti-mouse TCRγδ (GL3), PE-CF594	BD	Cat#563532; RRID:AB_2661844
Myeloid cells: anti-mouse B220 (RA3-6B2), PE-CF594	BD	Cat#562290; RRID:AB_11151901
Myeloid cells: anti-mouse NK1.1 (PK136), PE-CF594	BD	Cat#562864; RRID:AB_2737850
Myeloid cells: anti-mouse CD11b (M1/70), BV785	BioLegend	Cat#101243; RRID:AB_2561373
Myeloid cells: anti-mouse Ly-6G (1A8), PE-Cy7	BD	Cat#560601; RRID:AB_1727562
Myeloid cells: anti-mouse Siglec-F (E50-2440), BV421	BD	Cat#562681; RRID:AB_2722581
Myeloid cells: anti-mouse CD11c (N418), APC-eFluor 780	eBioscience	Cat#47-0114-82; RRID:AB_1548652
Myeloid cells: anti-mouse CD64 (X54-5/7.1), APC	BioLegend	Cat#139306; RRID:AB_11219391
Myeloid cells: anti-mouse MHC-II (M5/114.15.2), AF700	eBioscience	Cat#56-5321-82; RRID:AB_494009
Myeloid cells: anti-mouse CD103 (2E7), PerCP-eFluor 710	eBioscience	Cat#46-1031-82; RRID:AB_2573704
Myeloid cells: anti-mouse CD24 (M1/69), FITC	BioLegend	Cat#101805; RRID:AB_312838
Myeloid cells: anti-mouse Ly-6C (HK1.4), BV605	BioLegend	Cat#128036; RRID:AB_256235
Myeloid cells: anti-mouse CCR2 (475301), PE	R&D Systems	Cat#FAB5538P; RRID:AB_10718414
T cells and epithelial cells: anti-mouse CD45 (30-F11), APC-eFluor 780	eBioscience	Cat#47-0451-82; RRID:AB_1548781
T cells: anti-mouse CD90.2 (30-H12), BV785	BioLegend	Cat#105331; RRID:AB_2562900
T cells: anti-mouse TCRβ (H57-597), BUV737	BD	Cat#612821; RRID:AB_2870145
T cells: anti-mouse CD4 (RM4-5), BV510	BioLegend	Cat#100559; RRID:AB_2562608
T cells: anti-mouse FOXP3 (FJK-16 s), AF700	eBioscience	Cat#56-5773-82; RRID:AB_1210557
T cells: anti-mouse CD8β (H35-17.2), BV605	BD	Cat#740387; RRID:AB_2740117
T cells: anti-mouse IFN-γ (XMG1.2), eFluor 450	eBioscience	Cat#48-7311-82; RRID:AB_1834366
T cells: anti-mouse IL-17A (TC11-18H10.1), AF488	BioLegend	Cat#506910; RRID:AB_536012
T cells: anti-mouse IL-22 (1H8PWSR), PE	eBioscience	Cat#12-7221-82; RRID:AB_10597428

(*Continued on next page*)

Continued

REAGENT or RESOURCE	SOURCE	IDENTIFIER
Epithelial cells: anti-mouse EpCAM (G8.8), PE	eBioscience	Cat#12-5791-82; RRID:AB_953615
Epithelial cells: anti-mouse CD31 (MEC13.3), AF647	Biolegend	Cat#102516; RRID:AB_2161029
Bacterial and virus strains		
Yersinia pseudotuberculosis 32777 *ΔyopM*	Laboratory of Yasmine Belkaid	N/A
Klebsiella pneumoniae MKP103	Laboratory of Colin Manoil	N/A
Klebsiella pneumoniae MKP103 Tn mutant library	Ramage et al., 2017	N/A
Klebsiella pneumoniae MKP103 *cyxB*$^{-}$ (genotype: KPNIH1_14375-128::T30)	Ramage et al., 2017	strain: tnkp1_lr150117p11q128
Klebsiella pneumoniae MKP103 *pduQ*$^{-}$ (genotype: KPNIH1_21325-130::T30)	Ramage et al., 2017	strain: tnkp1_lr150124p03q130
Klebsiella pneumoniae MKP103 *acrE*$^{-}$ (genotype: KPNIH1_24010-122::T30)	Ramage et al., 2017	strain: tnkp1_lr150117p16q122
Klebsiella pneumoniae ATCC 43816	ATCC	N/A
Citrobacter rodentium ICC169	Laboratory of Gad Frankel	N/A
Citrobacter rodentium ICC169 *cydAB*$^{-}$	This paper	N/A
Bilophila wadsworthia ATCC 49260	Culture Collection University of Gothenburg	CCUG 32349T
E. coli S17-1 λ-pir	Laboratory of Andreas Bäumler	N/A
Chemicals, peptides, and recombinant proteins		
PBS	Corning	Cat#21-040-CM
LB agar (Lennox)	Sigma	Cat#L2897
2x YT broth	Sigma	Cat#Y1003
Yeast extract	Sigma	Cat#70161
Wilkins-Chalgren broth	Thermo Fisher	Cat#CM0643B
Agar	Sigma	Cat#A1296
Nutrient Broth	VWR	Cat#90002-660
MacConkey agar	VWR	Cat#95022-720
Bile esculin azide agar	Sigma	Cat#06105
Taurine	Sigma	Cat#T0625
Bismuth subsalicylate	Sigma	Cat#480789
Streptomycin	Sigma	Cat#S6501
Chloramphenicol	Alfa Aesar	Cat#B20841
Kanamycin	Sigma	Cat#K1377
Ampicillin	Sigma	Cat#A0166
Neomycin	Sigma	Cat#N6386
Vancomycin	Sigma	Cat#V1130
Nalidixic acid	Sigma	Cat#N8878
KH_2PO_4	Sigma	Cat#P5655
K_2HPO_4	Sigma	Cat#P3786
$NaNH_4HPO_4$	Sigma	Cat#S9506
$MgSO_4$	Sigma	Cat#M7506
$CaCl_2$	Sigma	Cat#C7902
$CoCl_2$	Sigma	Cat#C8661
$CuSO_4$	Sigma	Cat#209198
$MnSO_4$	Sigma	Cat#M7634
Na_2MoO_4	Sigma	Cat#M1003
Na_2SeO_3	Sigma	Cat#S5261

(*Continued on next page*)

Continued

REAGENT or RESOURCE	SOURCE	IDENTIFIER
$NiSO_4$	Sigma	Cat#227676
$ZnSO_4$	Sigma	Cat#Z0251
1,2-Propanediol	Sigma	Cat#134368
Sodium formate	Alfa Aesar	Cat#A17813
Sodium tetrathionate	Sigma	Cat#S5758
Sodium nitrate	Sigma	Cat#S5506
Dimethyl sulfoxide	Sigma	Cat#D2650
Trimethylamine N-oxide	Sigma	Cat#T0514
Sodium taurocholate	Sigma	Cat#T4009
Sodium hydrosulfide	Sigma	Cat#161527
1,4-Dihydroxy-2-naphthoic acid (DHNA)	Sigma	Cat#281255
$MgCl_2$	Sigma	Cat#M3634
Ferrous ammonium sulfate	Sigma	Cat#215406
5-bromo-4-chloro-3-indolyl phosphate (X-phos)	Sigma	Cat#203788
RPMI 1640	Corning	Cat#10-040-CV
Sodium pyruvate	Corning	Cat#25-000-CI
MEM nonessential amino acids	Corning	Cat#25-025-CI
L-glutamine	Corning	Cat#25-005-CI
HEPES	Corning	Cat#25-060-CI
Penicillin/streptomycin	Corning	Cat#30-002-CI
β-Mercaptoethanol (55 mM)	Thermo Fisher	Cat#21985023
Fetal bovine serum	Thermo Fisher	Cat#SH30070
EDTA	Corning	Cat#46-034-CI
DL-Dithiothreitol (DTT)	Sigma	Cat#D0632
Liberase TL	Sigma	Cat#5401020001
DNase I	Sigma	Cat#DN25
Percoll	VWR	Cat#89428
Fc Block	BD	Cat#553141
Counting beads	Thermo Fisher	Cat#NC9166302
Phorbol 12-myristate 13-acetate (PMA)	Sigma	Cat#P8139
Ionomycin	Sigma	Cat#I0634
GolgiPlug	BD	Cat#555029
HBSS	Corning	Cat#21-022-CV
Dulbecco's Modified Eagle Medium (DMEM)	Corning	Cat#10-017-CV
Dispase II	Thermo Fisher	Cat#17-105-041
DAPI	Sigma	Cat#D9542
RNAlater	Sigma	Cat#R0901
β-Mercaptoethanol (14.3 M)	Sigma	Cat#63689
Formalin	Sigma	Cat#HT501128
Carmine	Sigma	Cat#C1022
Methyl cellulose	Sigma	Cat#M7140
Critical commercial assays		
MagAttract PowerMicrobiome DNA/ RNA Kit	QIAGEN	Cat#27500-4-EP
Phusion High-Fidelity PCR Master Mix	Thermo Fisher	Cat#F531L
Illumina DNA Prep	Illumina	Cat#20018705
Taurine Assay Kit	Cell Biolabs	Cat#MET-5071

(*Continued on next page*)

Continued

REAGENT or RESOURCE	SOURCE	IDENTIFIER
Total Bile Acid Assay Kit	Cell Biolabs	Cat#STA-631
OxiSelect Free Hydrogen Sulfide Assay Kit	Cell Biolabs	Cat#XAN-5084
LIVE/DEAD Fixable Blue Dead Cell Staining Kit	Thermo Fisher	Cat#L23105
Fixation/Permeabilization Solution Kit	BD	Cat#554714
Foxp3/Transcription Factor Staining Buffer Set	eBioscience	Cat#00-5523-00
RNeasy Fibrous Tissue Mini Kit	QIAGEN	Cat#74704
RNeasy Plus Micro Kit	QIAGEN	Cat#74034
High Sensitivity RNA ScreenTape	Agilent	Cat#5067-5579
Universal Plus mRNA-Seq Library Preparation Kit	Tecan Genomics	Cat#0520
Ovation SoLo RNA-Seq Library Preparation Kit	Tecan Genomics	Cat#0501
Deposited data		
Raw 16S, metagenomics, RNA-seq, and Tn-seq data	This study	SRA: PRJNA666931
Raw 16S data	Fonseca et al., 2015	SRA: PRJNA276477
Raw metagenomics data	Rosshart et al., 2017	SRA: PRJNA390686
Experimental models: organisms/strains		
Mouse: SPF C57BL/6	Taconic Biosciences	C57BL/6NTac
Mouse: SPF B6.SJL-Ptprc^{a}/ BoyAiTac (CD45.1)	NIAID-Taconic exchange contract	Tac 8478
Mouse: SPF wildR C57BL/6	Laboratory of Barbara Rehermann or Taconic Biosciences	N/A
Mouse: Germ-free C57BL/6NTac	NIAID Gnotobiotic Animal Facility	N/A
Oligonucleotides		
515F: TCGTCGGCAGCGTCAGATGTG TATAAGAGACAGGTGCCAGCMGCCGC GGTAA	Caporaso et al., 2012	N/A
806R: GTCTCGTGGGCTCGGAGATGTG TATAAGAGACAGGGACTACHVGGGTW TCTAAT	Caporaso et al., 2012	N/A
Tn-seq primer: PCR-1: biotin-GCCATAAC TTCGTATAGCATACATTATACGAAGTTAT GCGAGCTC	This study	N/A
Tn-seq primer: PCR-1: GTGACTGGAG TTCAGACGTGTGCTCTTCCGATCTGG GGGGGGGGGGGGGG	This study	N/A
Tn-seq primer: PCR-2: AATGA TACGGCGACCACCGAGATCTACACTC TTTCCCTACACGACGCTCTTCCGATC TNNNNNCCAACAAGAGCTTCAGGG TTGAG (N, random base)	This study	N/A
Tn-seq primer: PCR-2: CAAGCAGAAGACGGCATACGAGAT[BC] GTGACTGGAGTTCAGACGTGTG ([BC], 6 base Illumina barcode)	This study	N/A
Recombinant DNA		
Plasmid: pCAL60	Laboratory of Andreas Bäumler; Lopez et al., 2016	N/A

(*Continued on next page*)

Continued

REAGENT or RESOURCE	SOURCE	IDENTIFIER
Software and algorithms		
QIIME 2	Bolyen et al., 2019	https://qiime2.org/
JAMS	https://github.com/johnmcculloch/JAMS_BW	N/A
Trimmomatic	Bolger et al., 2014	http://www.usadellab.org/cms/?page=trimmomatic
Bowtie 2	Langmead and Salzberg, 2012	http://bowtie-bio.sourceforge.net/bowtie2/index.shtml
Megahit	Li et al., 2015	https://github.com/voutcn/megahit
Prokka	Seemann, 2014	https://github.com/tseemann/prokka
Kraken 2	Wood et al., 2019	https://ccb.jhu.edu/software/kraken2/
Cutadapt	Martin, 2011	https://cutadapt.readthedocs.io/en/stable/
Rsubread	Liao et al., 2019	https://bioconductor.org/packages/release/bioc/html/Rsubread.html
DESeq2	Love et al., 2014	https://bioconductor.org/packages/release/bioc/html/DESeq2.html
KEGG Automatic Annotation Server	Moriya et al., 2007	https://www.genome.jp/kegg/kaas/
FACSDiva	BD	N/A
FlowJo	Treestar	N/A
STAR	Dobin et al., 2013	https://github.com/alexdobin/STAR
Homer	Heinz et al., 2010	http://homer.ucsd.edu/homer/ngs/
Metascape	Zhou et al., 2019	https://metascape.org/gp/index.html#/main/step1
Mouse Genome Informatics	Bult et al., 2019	http://www.informatics.jax.org/vocab/gene_ontology
Fiji	Schindelin et al., 2012	https://imagej.net/Fiji
SPAdes	Bankevich et al., 2012	https://cab.spbu.ru/software/spades/
Prism	GraphPad	N/A
R	https://www.r-project.org/	N/A
Other		
96-well plates	Sigma	Cat#CLS3799
Microaerophilic sachets	Thermo Fisher	Cat#R681005
Polycarbonate membranes	Sigma	Cat#WHA110606
Zirconia/silica beads	Thermo Fisher	Cat#NC0362415
Tubes with 1.5 mm zirconium beads	Sigma	Cat#Z763799

RESOURCE AVAILABILITY

Lead contact

Further information and requests for resources and reagents should be directed to and will be fulfilled by the Lead Contact, Yasmine Belkaid (ybelkaid@niaid.nih.gov).

Materials availability

The *C. rodentium cydAB*$^{-}$ mutant and the *E. faecalis* strains isolated in this study are available upon request.

Data and code availability

Original 16S, shotgun metagenomics, RNA-seq, and Tn-seq datasets generated during this study are available at the Sequence Read Archive: (PRJNA666931). The published 16S dataset for mice previously infected with the *Y. pseudotuberculosis* WT and

the 16S and metagenomics datasets for generation F2 wildR mice are also available at the Sequence Read Archive: PRJNA276477, PRJNA390686. An unpublished in-house package, JAMS, used to analyze metagenomics and whole-genome sequencing data is available at https://github.com/johnmcculloch/JAMS_BW.

EXPERIMENTAL MODEL AND SUBJECT DETAILS

Mice

Conventional SPF C57BL/6 and congenic CD45.1 mice (used interchangeably) were acquired from Taconic Biosciences (only barriers positive for segmented filamentous bacteria) and maintained at NIAID or NIDDK animal facilities. WildR SPF C57BL/6 mice were created, bred, and maintained at an NIDDK animal facility (Rosshart et al., 2017), then transferred entirely to Taconic Biosciences. The F10 wildR mice in this study were analyzed after wildR mice had been re-imported from Taconic Biosciences to NIDDK. GF C57BL/6 mice were bred and maintained at the NIAID Microbiome Program Gnotobiotic Animal Facility. All facilities were accredited by the Association for Assessment and Accreditation of Laboratory Animal Care (AAALAC) International, and all animal procedures were performed in accordance with the Guide for the Care and Use of Laboratory Animals under animal study proposals approved by the NIAID or NIDDK Animal Care and Use Committees. Sex- and age-matched mice between 6-20 weeks of age were used for all experiments. Female and male mice were used for experiments with wildR and GF mice, while only female mice were used for experiments involving only conventional mice.

Bacteria

The *Y. pseudotuberculosis*, *Kpn*, *C. rodentium*, and *B. wadsworthia* WT strains were 32777, MKP103 (a KPNIH1 derivative with the KPC-3 carbapenemase-encoding gene deleted (Ramage et al., 2017)), ICC169 (an ICC168 derivative resistant to nalidixic acid), and ATCC 49260. The *Kpn cyxB*$^{-}$, *pduQ*$^{-}$, and *acrE*$^{-}$ Tn mutants were purified from the MKP103 Tn mutant library (Ramage et al., 2017) and confirmed via PCR. *Y. pseudotuberculosis ΔyopM* (Han et al., 2017) was routinely revived on LB agar and cultured in 2x YT broth at 25°C with shaking at 200-250 rpm. *Kpn* and *C. rodentium* WT and mutant strains were routinely revived on LB agar and cultured in LB broth (10 g/l tryptone, 5 g/l yeast extract, 8 g/l NaCl) at 37°C with shaking at 200 rpm. *B. wadsworthia* was routinely revived on Wilkins-Chalgren agar + 50 mM taurine and cultured in Wilkins-Chalgren broth + 50 mM taurine at 37°C without shaking in an anaerobic chamber (Whitley Workstation A85).

METHOD DETAILS

Intestinal infection of mice with gut pathogens

Overnight (12-14 hour) *Y. pseudotuberculosis ΔyopM* cultures were resuspended in PBS, adjusted to an absorbance at 600 nm (A_{600}) of 0.1 in PBS, and gavaged into mice fasted overnight for 13-15 hours (~2×10^7 CFU in 200 μl/mouse). Overnight *Kpn* cultures were resuspended in LB, adjusted to an A_{600} of 1 in LB, and gavaged into overnight-fasted mice (~2×10^8 CFU in 200 μl/mouse). Overnight *C. rodentium* cultures were resuspended in PBS, adjusted to an A_{600} of 5 or 25, and gavaged into non-fasted mice (~1 or 5×10^9 CFU in 200 μl/mouse). For *C. rodentium* experiments, mouse cages were not changed from 3-5 days before infection until 5 days after infection. For *in vivo* competition experiments, the same procedures as described above were followed, except that the WT and mutant were mixed together at a 1:1 ratio prior to gavage. When pelleting cultures, all bacteria were centrifuged at 3-4,000 x g for 2-5 minutes at room temperature. All absorbances were measured with a spectrophotometer (Biochrom).

Treatment of mice with taurine, bismuth, and streptomycin

To treat mice with taurine, mice were placed onto non-acidified tap water + 200 mM taurine for 2-3 weeks prior to infection, during which fresh water was provided every 3-5 days. At the same as when mice were first placed onto taurine water, mice were exchanged between paired control and treatment cages, the intent being to reduce microbiota variability between cages (generally, 2 mice in a control cage of 5 mice were exchanged with 2 mice in a treatment cage of 5 mice). Starting the evening (12-14 hours) prior to *Kpn* infection, mice were placed onto non-acidified tap water lacking taurine, to avoid stimulation of *Kpn* growth by taurine. To treat mice with bismuth, starting the evening prior to infection, mice were placed onto non-acidified tap water + 20 mM bismuth subsalicylate and maintained on bismuth water throughout the course of infection. To treat mice with streptomycin, mice were gavaged with 20 mg streptomycin (200 μl of a freshly prepared 100 mg/ml solution) 1 day prior to infection.

Collection and processing of gut samples to determine CFU

Fecal pellets (colon lumen samples) were collected directly from mice or by placing mice into paper cups. Cecum lumen samples were collected by squeezing out the contents of extracted ceca using forceps. Mucosal samples were collected by cutting extracted tissues (colons, ceca, or ilea) open longitudinally, thoroughly rinsing tissues in Petri dishes with PBS, scraping the interior surface of rinsed tissues using closed forceps, and collecting the scrapings (mucosa). The PBS used to rinse ileal tissues was transferred to 50 mL conical tubes and centrifuged at 4,000 rpm (2,880 x g) for 5 minutes at room temperature to collect the pellets (ileum lumen

samples). All gut samples were transferred or collected directly into pre-weighed 1.5 mL tubes, weighed after collection, homogenized in 500 μl PBS using a pipette tip, and vortexed for 5 s. After allowing large particles to settle, top fractions were collected to determine CFU.

Determination of CFU

CFU were determined for both gut samples and *in vitro* growth assays as described using a multichannel pipette (Hung et al., 2009). Briefly, samples were serially diluted in 96-well plates with PBS, and 10 μl of each dilution was spotted 5 times onto LB agar (1 plate per sample, 50 μl per dilution). For *in vitro* growth assays, LB without antibiotics was used to determine total CFU; LB + 175 μg/ml chloramphenicol, *Kpn* Tn mutant CFU; LB + 100 μg/ml kanamycin, *C. rodentium cydAB*$^-$ CFU. For gut samples, LB + 50 μg/ml ampicillin + 100 μg/ml neomycin + 100 μg/ml vancomycin was used to determine total *Kpn* CFU; the same media + 175 μg/ml chloramphenicol, *Kpn* Tn mutant CFU; LB + 50 μg/ml nalidixic acid, total *C. rodentium* CFU (only large colonies); the same media + 100 μg/ml kanamycin, *C. rodentium cydAB*$^-$ CFU. In competition assays, samples with fewer than 10 total CFU were excluded from final results.

Preparation of NCE medium

No carbon E (NCE) minimal medium (Faber et al., 2017) for *in vitro* growth assays (below) was prepared from stock solutions in diH_2O: 1) 10x salts (at 1x, 29 mM KH_2PO_4, 28.3 mM K_2HPO_4, 16.7 mM $NaNH_4HPO_4$), 2) 1000x $MgSO_4$ (at 1x, 1 mM), and 3) 1000x trace metals (at 1x, 0.3 μM $CaCl_2$, 3 μM $CoCl_2$, 0.1 μM $CuSO_4$, 2 μM $MnSO_4$, 0.2 μM Na_2MoO_4, 0.2 μM Na_2SeO_3, 0.1 μM $NiSO_4$, 0.1 μM $ZnSO_4$).

Kpn and C. rodentium *in vitro* growth assays

All overnight cultures for growth assays were grown without shaking in an anaerobic chamber, diluted 1:250 into test media that was pre-reduced overnight in the anaerobic chamber, and further grown for 23-25 hours in either the anaerobic chamber, a hypoxic chamber (Baker Ruskinn PhO_2x Box) with 0.8% oxygen, an anaerobic jar with a microaerophilic sachet (6%–12% oxygen), or in air (21% oxygen) prior to determining CFU. To assess electron acceptor usage, overnight cultures in LB were diluted into NCE + 5 mM 1,2-propanediol + 50 mM electron acceptor or vehicle (water). For *in vitro* competition experiments, WT and mutant overnight cultures in NCE + 0.2% yeast extract + 50 mM carbon source (1,2-propanediol or formate) were mixed together at a 1:1 ratio and diluted into NCE + 5 mM carbon source. For inhibition assays, overnight cultures in NCE + 0.2% yeast extract + 50 mM carbon source (1,2-propanediol or formate) were diluted into NCE + 5 mM carbon source + 5 mM taurocholate, 5 mM taurine, sodium hydrosulfide (0.125-1 mM for *Kpn* or 1-5 mM for *C. rodentium*), or vehicle (water). Sodium hydrosulfide was freshly prepared for all experiments.

B. wadsworthia *in vitro* growth assays

To assess sulfur source usage, *B. wadsworthia* was grown overnight in pre-reduced Wilkins-Chalgren broth + 50 mM taurine without shaking in an anaerobic chamber, diluted 1:500 into pre-reduced Wilkins-Chalgren broth + 50 mM sulfur source (taurine or magnesium sulfate) or vehicle (water), and further grown overnight in the anaerobic chamber prior to measuring A_{600}. To assess growth stimulation by DHNA, overnight cultures in NCE (with 1 mM $MgCl_2$ rather than $MgSO_4$) + 50 mM taurine + 50 mM formate were diluted 1:500 into the same medium + 276 μg/ml ferrous ammonium sulfate + 200 μg/ml DHNA or vehicle (ethanol) and further grown in the anaerobic chamber.

Construction of C. rodentium cydAB mutant

To delete *cydAB* from *C. rodentium* ICC169, pCAL60, a plasmid previously constructed to delete *cydAB* from *C. rodentium* DBS100, was used (Lopez et al., 2016). This plasmid contains 1) a kanamycin resistance cassette flanked by the regions up and downstream of *cydAB*, 2) a chloramphenicol resistance cassette on the backbone, and 3) to allow for blue/white screening, the *Salmonella* Typhimurium *phoN* gene on the backbone. To conjugate pCAL60 from *E. coli* S17-1 λ-pir (donor) into *C. rodentium* ICC169 (recipient), overnight cultures of the recipient (diluted 1:10 into fresh LB) and donor (not diluted) were resuspended in fresh LB, mixed 1:1, and spotted onto polycarbonate membranes (100 μl/membrane) placed onto LB agar. After 4-6 hours, conjugations were resuspended in 1 mL LB and struck onto LB agar with 50 μg/ml nalidixic acid (to select against *E. coli* S17-1 λ-pir), 100 μg/ml kanamycin (to select for single crossover events), and 40 μg/ml X-phos (to screen for double crossover events). White colonies were screened for sensitivity to 15 μg/ml chloramphenicol, and sensitive colonies were confirmed for *cydAB* deletion via PCR.

Lung infection of mice with Kpn

For lung infections, *Kpn* ATCC 43816 was used since this strain is highly virulent in lung infection models (Broberg et al., 2014). *Kpn* was inoculated directly from a freezer stock into 50 mL Nutrient broth and cultured for 7 hours at 37°C with shaking at 200 rpm. Mice anesthetized with isoflurane were intratracheally inoculated with 3×10^3 CFU in 80 μl. After 36 hours, lungs were harvested into pre-weighed tubes with PBS (1 ml/lung) and 1.5 mm zirconium beads, weighed after collection, homogenized at 5,000 rpm for 2 20 s cycles using a Precellys 24 (Bertin Instruments), and plated onto MacConkey agar to determine CFU.

Preservation of microbiota

Fecal samples from post-*ΔyopM* mice were frozen at −80°C prior to being processed, while samples from taurine-treated mice were processed shortly after being collected. Samples were transferred into an anaerobic chamber, homogenized in pre-reduced PBS (~20 μl/mg feces) using a pipette tip, and vortexed for 5 s. After allowing large particles to settle, top fractions were diluted 1:5 into pre-reduced PBS, mixed 1:1 with pre-reduced 20% glycerol, aliquoted, and stored at −80°C. Prior to gavage into GF mice, aliquots were thawed in the anaerobic chamber and mixed 1:1 with pre-reduced PBS.

Conventionalization of GF mice

GF mice were transferred using aseptic technique into sterile cages with acidified drinking water, immediately gavaged with 200 μl microbiota (revived in 5% glycerol, as described in the previous section), housed under SPF conditions, and gavaged twice more with microbiota on consecutive days. To pre-engraft GF mice with *B. wadsworthia*, mice were 1) aseptically transferred to SPF cages, 2) immediately gavaged with 200 μl of concentrated *B. wadsworthia* (an overnight 25 mL culture resuspended in 1-2 mL Wilkins-Chalgren broth), 3) gavaged the following day again with *B. wadsworthia*, 4) hours after the second *B. wadsworthia* gavage, gavaged with 200 μl SPF microbiota (freshly prepared by homogenizing fecal pellets in pre-reduced PBS in an anaerobic chamber), 5) gavaged the following day again with freshly prepared SPF microbiota. After conventionalization, mice were rested for 1.5-2 weeks prior to infection, during which cages were only changed if necessary (e.g., if water bottles leaked). Starting the evening before infection, mice were placed onto non-acidified tap water.

16S rRNA gene profiling

DNA was extracted from fecal pellets using phenol:chloroform (Goodman et al., 2011) or the MagAttract PowerMicrobiome DNA/RNA Kit. 16S V4 rDNA libraries were prepared using the Phusion High-Fidelity PCR Master Mix with primers 515F and 806R (Caporaso et al., 2012), and sequenced on an Illumina MiSeq instrument by the NIAID Microbiome Program core facility, with the exception of fecal pellets from F10 wildR mice, which were processed and sequenced by the NCI Cancer and Inflammation Program Microbiome and Genetics Core.

16S data were analyzed using QIIME 2 (Bolyen et al., 2019). Briefly, reads were denoised using the q2-dada2 plugin (exact parameters were forward reads truncated to 180 bases with 20 bases trimmed from the 5′ end, reverse reads truncated to 150 bases with 20 bases trimmed from the 5′ end, and bases truncated with quality score below 10). Using the q2-feature-table plugin, samples within an experiment were rarefied to the depth of the sample with the fewest reads (> 19,000 reads for all experiments), and sequence variants were filtered if within an experiment they did not occur in at least 3 samples. Rooted phylogenetic trees were generated using the align-to-tree-mafft-fasttree method in the q2-phylogeny plugin. Alpha and beta diversity analyses were performed using the core-metrics-phylogenetic method in the q2-diveristy plugin, with a sampling depth of 5,000 reads. Taxonomy was assigned to sequence variants using the q2-feature-classifier plugin and a naive Bayes classifier pre-trained on the SILVA 132 515F/806R 99% OTUs (Yilmaz et al., 2014) provided as a QIIME 2 data resource. A pseudocount was applied prior to calculating differences in the relative abundance of taxonomic groups. In parallel, the same workflow was used to re-analyze published 16S data for fecal pellets from post-*Yptb* WT mice (Fonseca et al., 2015) and published 16S data for ileocecal material from F2 labR and F2 wildR mice (Rosshart et al., 2017).

Shotgun metagenomics

Metagenomics libraries were generated using the Illumina DNA Prep kit, with 500 ng purified DNA as template, and sequenced on an Illumina NextSeq instrument (average depth per sample, 3.6 Gb; range, 2.7-4.5 Gb) by the NIAID Microbiome Program core facility.

Data were analyzed using an in-house package (https://github.com/johnmcculloch/JAMS_BW) as described (Rosshart et al., 2019). In parallel, the same package was used to re-analyze published metagenomics data for ileocecal material from F2 labR and F2 wildR mice (Rosshart et al., 2017). Briefly, sequencing reads were processed using Trimmomatic (Bolger et al., 2014); host-derived reads were filtered using Bowtie 2 (Langmead and Salzberg, 2012); microbiota-derived reads were assembled into contigs using Megahit (Li et al., 2015); genes within contigs were predicted and annotated with EC numbers using Prokka (Seemann, 2014); the relative abundance of EC numbers was determined by aligning microbiota-derived reads back to contigs using Bowtie 2; contigs and unassembled reads were taxonomically classified by k-mer analysis using Kraken 2 (Wood et al., 2019) and, as reference, a custom-built database of all genome sequences in GenBank. The relative contribution of taxa to individual EC numbers was determined by tallying the read coverage of each single gene with a particular EC number and obtaining the taxonomic information for that single gene from the Kraken 2 identification of the exact contig in which the gene was predicted *ab initio*.

Of note, for many of the functions in Figure 2, more than one species of *Desulfovibrio* was often identified as contributing to each function. However, based on 16S analysis, all post-*ΔyopM* samples were determined to contain only a single species of *Desulfovibrio*. Thus, the metagenomic identification of multiple species of *Desulfovibrio* was deemed an artifact due to the relatively low depth of *Desulfovibrio*-derived sequencing reads. Because of this, the multiple species of *Desulfovibrio* identified as contributing to each function in Figure 2 were aggregated into a single unidentified *Desulfovibrio* species.

Profiling of metabolites by mass spectrometry

Cecal contents collected onto dry ice were submitted to the West Coast Metabolomics Center at the University of California, Davis. The relative abundance of 449 metabolites (186 defined, 263 undefined) was quantified using gas chromatography time-of-flight mass spectrometry (GC-TOF-MS). The absolute abundance of 23 bile acids was quantified using liquid chromatography-mass spectrometry (LC-MS).

Measurement of fecal taurine and total bile acids

Fecal taurine and total bile acids were measured using colorimetric assay kits (Cell Biolabs) according to the manufacturer's instructions, except that 1) all reagent volumes were halved, and 2a) fecal samples were collected into pre-weighed tubes with PBS (10 μl/mg feces) and 0.1 mm zirconia/silica beads, 2b) homogenized at 5,000 rpm for 3 20 s cycles using a Precellys 24 (Bertin Instruments), and 2c) centrifuged at 10,000 x g for 2 minutes to collect supernatants. Fecal pellets for measuring taurine and total bile acids were collected in the morning.

Measurement of sulfide production by *ex vivo* microbiota cultures

Sulfide production by *ex vivo* microbiota cultures was measured using the OxiSelect Free Hydrogen Sulfide Assay Kit. Briefly, freshly collected fecal samples were transferred into an anaerobic chamber, homogenized in pre-reduced PBS (~20 μl/mg feces) using a pipette tip, and vortexed for 5 s. To establish *ex vivo* cultures, the top fraction of fecal homogenates was diluted 1:1 with pre-reduced PBS, and 225 μl was transferred into non-adjacent wells of a 96-well plate containing 25 μl vehicle (0.5 M NaCl) or 25 μl 0.5 M taurine and 0.5 M sodium formate. The areas of the 96-well plate lid directly above sample wells were each coated with 20-25 μl of the Lid Coating Mix, according to the manufacturer's instructions, and after placing the lid over the cultures, it was removed at 15-20 minute intervals from the anaerobic chamber to measure absorbance at 405 nm on a plate reader (BioTek Synergy HTX). Standard curves were generated using freshly prepared sodium hydrosulfide and measured in the same plates as *ex vivo* cultures.

Tn-seq

The *Kpn* MKP103 Tn mutant library (Ramage et al., 2017) arrayed into 96-well plates was revived overnight in LB at 37°C without shaking, combined into a single pool, mixed 1:1 with 50% glycerol, and stored as aliquots at −80°C. Thawed aliquots were grown overnight (12-14 hours) and prepared for gavage as described above for routine *Kpn* infections. DNA extracted from fecal samples collected at 8 hours post-infection was used as template in the 2-PCR method for generating Tn-seq sequencing libraries, according to a published protocol (Stacy et al., 2016), except with primers designed for the *Kpn* Tn mutant library. Briefly, DNA was C-tailed using terminal deoxynucleotidyl transferase, PCR-amplified with a biotinylated primer targeting the Tn sequence and a primer targeting the C-tail (PCR-1), purified with streptavidin-coated magnetic beads, further PCR-amplified to append forward and reverse Illumina adaptor sequences (PCR-2), and sequenced on an Illumina NextSeq instrument by the NCI Cancer and Inflammation Program Microbiome and Genetics Core.

Tn-seq data were analyzed largely as described (Stacy et al., 2016). 1) Reads were processed as follows using Cutadapt (Martin, 2011): a) the exact Tn sequence ATGTGTATAAGAGACAG was trimmed from 5′ ends (this quality-control sequence should be amplified by the second Tn-specific forward primer immediately prior to *Kpn* DNA), b) C-tails and low-quality bases (Q < 20) were trimmed from 3′ ends, and c) reads were trimmed to 20-25 bases in length. 2) Processed reads were mapped to the KPNIH1 genome using Bowtie 2 (default end-to-end alignment) (Langmead and Salzberg, 2012). 3) In Unix, a) low-quality alignments (Q < 39) were filtered, b) the number of unique Tn per sample was tallied (in doing so, the 9 base duplication of the Tn5 target sequence (Goryshin et al., 1998) was trimmed from alignments mapping to the negative strand), c) to achieve a uniform density of 5,000-6,000 Tn per sample, samples with < 5,000 Tn were concatenated, and samples with > 6,000 Tn were rarefied (alignments were discarded), and d) the relative abundance per unique Tn was tallied for each sample. 4) The relative Tn abundance per gene was tallied for each sample using Rsubread (Liao et al., 2019). 5) Samples were normalized for differences in sequencing depth using DESeq2 (Love et al., 2014), and differential Tn abundance per gene was assessed using the DESeq2 Wald test. The KPNIH1 genome was annotated with K numbers using the KEGG Automatic Annotation Server (Moriya et al., 2007).

Processing of large intestines and livers for flow cytometry

To isolate cells from large intestinal lamina propria, large intestines (LI, colons with ceca) were extracted with minimal attached fat into complete medium (RPMI 1640 supplemented with 1 mM pyruvate, 0.1 mM nonessential amino acids, 2 mM glutamine, 20 mM HEPES, 100 U/ml penicillin, 0.1 mg/ml streptomycin, and 50 μM β-mercaptoethanol) + 3% fetal bovine serum (FBS) on ice. LI were cut open longitudinally, thoroughly rinsed in PBS to remove feces, cut into 1-2 cm pieces, and incubated in 10 mL complete medium + 3% FBS + 5 mM EDTA + 1 mM DTT for 20 minutes at 37°C with stirring. To remove epithelial cells, LI were next vigorously shaken in 10-15 mL complete medium + 2 mM EDTA in 50 mL conical tubes for 15-20 s and strained. After performing this procedure 3 times (each time with fresh media), LI were minced into fine pieces with scissors and digested in 10 mL complete medium + 0.1 mg/ml Liberase TL + 0.5 mg/ml DNase I for 25-30 minutes at 37°C with stirring. Digestions were stopped with 10 mL ice-cold complete medium + 3% FBS, passed through 70-μm filters, centrifuged at 1500 rpm for 5 minutes, resuspended in 4 mL 37.5% Percoll, centrifuged at 1800 rpm for 5 minutes, and resuspended in 300 μl complete medium + 3% FBS.

To isolate cells from livers, livers were disassociated through 70-μm filters with 4-6 mL complete medium, centrifuged at 1500 rpm for 5 minutes, resuspended in 10 mL 37.5% Percoll, centrifuged at 1800 rpm for 5 minutes, and resuspended in 300 μl complete medium + 3% FBS.

Flow cytometry

To assess myeloid cells, 100 μl of 300 μl single-cell suspensions were stained on ice for 15 minutes in PBS with fluorochrome-conjugated antibodies (against CD45 diluted 1:300; TCRβ, 1:400; TCRγδ, 1:400; B220, 1:400; NK1.1, 1:400; CD11b, 1:200; Ly-6G, 1:500; Siglec-F, 1:300; CD11c, 1:200; CD64, 1:200; MHC-II, 1:1000; CD103, 1:200; CD24, 1:500; Ly-6C, 1:400; CCR2, 1:100), fixable live/dead stain, Fc Block, and counting beads (to quantify cell numbers) and fixed on ice for at least 1 hour using the Fixation/Permeabilization Solution Kit.

To assess T cells, 200 μl of 300 μl single-cell suspensions were restimulated *in vitro* in complete medium + 10% FBS + 50 ng/ml PMA (phorbol 12-myristate 13-acetate) + 1 mM ionomycin + 1 μl/ml GolgiPlug for 2.5 hours at 37°C, stained on ice for 15 minutes in PBS with fluorochrome-conjugated antibodies against surface targets (CD45 diluted 1:500; CD90.2, 1:400; TCRβ, 1:200; CD4, 1:200; CD8β, 1:400), fixable live/dead stain, Fc Block, and counting beads (to quantify cell numbers), fixed on ice for at least 1 hour using the Foxp3/Transcription Factor Staining Buffer Set, and stained at room temperature for at least 30 minutes with antibodies against intracellular targets (Foxp3 diluted 1:100; IFN-γ, 1:100; IL-17A, 1:100; IL-22, 1:100; TCRβ, 1:200; CD4, 1:200). Cells were acquired on a BD LSRFortessa running FACSDiva software, and data were analyzed using FlowJo.

Processing of large intestines for epithelial cell sorting

Extracted large intestines (LI, colons with ceca) were cut open longitudinally, thoroughly rinsed in gut wash buffer (HBSS supplemented with 1 mM pyruvate, 1 mM nonessential amino acids, 2 mM glutamine, 20 mM HEPES, 100 U/ml penicillin, and 100 mg/ml streptomycin) + 2% FBS to remove feces, and cut into 1-2 cm pieces. Subsequently, LI were incubated in 10 mL gut wash buffer + 1 mM DTT for 7-8 minutes in a 37°C water bath, vigorously shaken, and strained to discard DTT-containing fractions. After performing this procedure 2 times, LI were incubated in 10 mL gut wash buffer + 5 mM EDTA for 7-8 minutes in a 37°C water bath, vigorously shaken, and strained to collect EDTA-containing fractions. After performing this procedure 2 times, the pooled EDTA-containing fractions were passed through 100-μm filters, centrifuged at 1,000 rpm for 5 minutes, washed with DMEM, and digested in 10 mL DMEM + 0.1 U/ml Dispase II + 0.1 mg/ml DNase I for 8 minutes in a 37°C water bath. Digestions were stopped with DMEM + 2.5% FBS, centrifuged at 1,000 rpm for 5 minutes, and washed with gut wash buffer. Cells were stained on ice for 30 minutes in gut wash buffer + 5% FBS with fluorochrome-conjugated antibodies (against EpCAM diluted 1:500; CD45, 1:1000; CD31, 1:200) and DAPI, and epithelial cells were sorted directly into Buffer RLT using a Sony MA900 (sorting chip size, 100 μm).

Liver and gut epithelial cell RNA-seq

Per liver, small pieces (0.5-1 cm in width) from the edge of each lobe were collected together into 1 mL RNAlater, incubated overnight at room temperature, and stored at −20°C. RNA was extracted using the RNeasy Fibrous Tissue Mini Kit according to the manufacturer's instructions, with the exceptions that 1a) samples were transferred to tubes with 1 mL Buffer RLT and 1.5 mm zirconium beads and 1b) homogenized at 5,000 rpm for 3 20 s cycles using a Precellys 24 (Bertin Instruments), and 2) only 50 μl of the homogenate was mixed with 250 μl fresh Buffer RLT + β-mercaptoethanol (14.3 M) and used to extract RNA. For sorted gut epithelial cells, RNA was extracted using the RNeasy Plus Micro Kit. The integrity of extracted RNA was assessed using an Agilent TapeStation. RNA-seq libraries were prepared using the Universal Plus mRNA-Seq Library Preparation Kit (for liver RNA) or the Ovation SoLo RNA-Seq Library Preparation Kit (for epithelial cell RNA) and sequenced on an Illumina NextSeq instrument by the NIH Center for Human Immunology core facility.

RNA-seq data were mapped to the mm10 mouse genome using STAR (default parameters) (Dobin et al., 2013). Samples with clonality greater than 2.5 as assessed by HOMER (Heinz et al., 2010) were excluded. Gene expression was assessed using HOMER's analyzeRepeats.pl with the options rna, mm10, -count exons, -condenseGenes, and differential gene expression was assessed using DESeq2 (Love et al., 2014). The enrichment of GO terms was assessed using Metascape (Zhou et al., 2019). Ribosomal protein and antimicrobial peptide annotations were obtained from the Gene Ontology Browser of the Mouse Genome Informatics website (Bult et al., 2019).

Measurement of gallbladder weight

Gallbladders were carefully extracted into PBS, and any attached fat was removed in a Petri dish using forceps and a scalpel. Prior to being weighed, gallbladders were blotted onto absorbent wipes to remove PBS. Gallbladders that leaked either during extraction or fat removal were excluded from final results.

Liver and colon histology

Liver samples (part of the largest lobe) and colon samples (distal 0.5-1 cm without feces) were fixed in 1 mL 10% neutral buffered formalin and submitted to Histoserv, Inc. for paraffin sectioning and H&E staining. Sections were imaged on a Leica SCN400 slide scanner and analyzed in a blinded manner, liver sections by a trained pathologist and colon sections using Fiji (Schindelin et al., 2012). The crypt length per mouse was assessed by averaging the length of 20 crypts per colon section.

Measurement of intestinal transit time

As previously described (Dey et al., 2015), non-fasted mice were gavaged with 200 μl carmine solution (6% (w/v) carmine in a 0.5% (w/v) methyl cellulose solution), and feces was collected every 30 minutes to assess for the presence of carmine, by streaking the collected feces onto a white paper towel. The time from gavage to the initial appearance of carmine in feces was recorded as the intestinal transit time.

E. faecalis isolation, identification, and whole-genome sequencing

The feces of 2 non-co-housed bismuth-treated mice was homogenized in PBS and struck onto bile esculin azide agar. Four colonies (2 colonies per mouse) were re-struck onto the same media and submitted to the NIAID Research Technologies Branch for species-level identification using a Bruker MALDI Biotyper. All 4 colonies were identified as *E. faecalis*. Whole-genome sequencing libraries were prepared using the Illumina DNA Prep kit and sequenced on an Illumina MiSeq instrument. Data were analyzed using the same in-house package as for metagenomics data, with SPAdes as the genome assembler (Bankevich et al., 2012).

QUANTIFICATION AND STATISTICAL ANALYSIS

The statistical details of experiments can be found in the figure legends. Reported n are the total samples (mice or cultures) per group; fold changes are the medians of pooled experiments; n.s., not significant; †$p < 0.1$; *$p < 0.05$; **$p < 0.01$; ***$p < 0.001$. Unless otherwise stated, p values were not corrected for multiple testing. Mann-Whitney tests (all unpaired and two-tailed) were performed in Prism or R; Grubbs' and ROUT outlier tests were performed in Prism; Benjamini-Hochberg corrections, hypergeometric tests, Kruskal-Wallis tests and PERMANOVA (QIIME 2 package), and Wald tests (DESeq2 package) were performed in R; Student's t tests (all unpaired and two-tailed) were performed in Prism.

Supplemental Figures

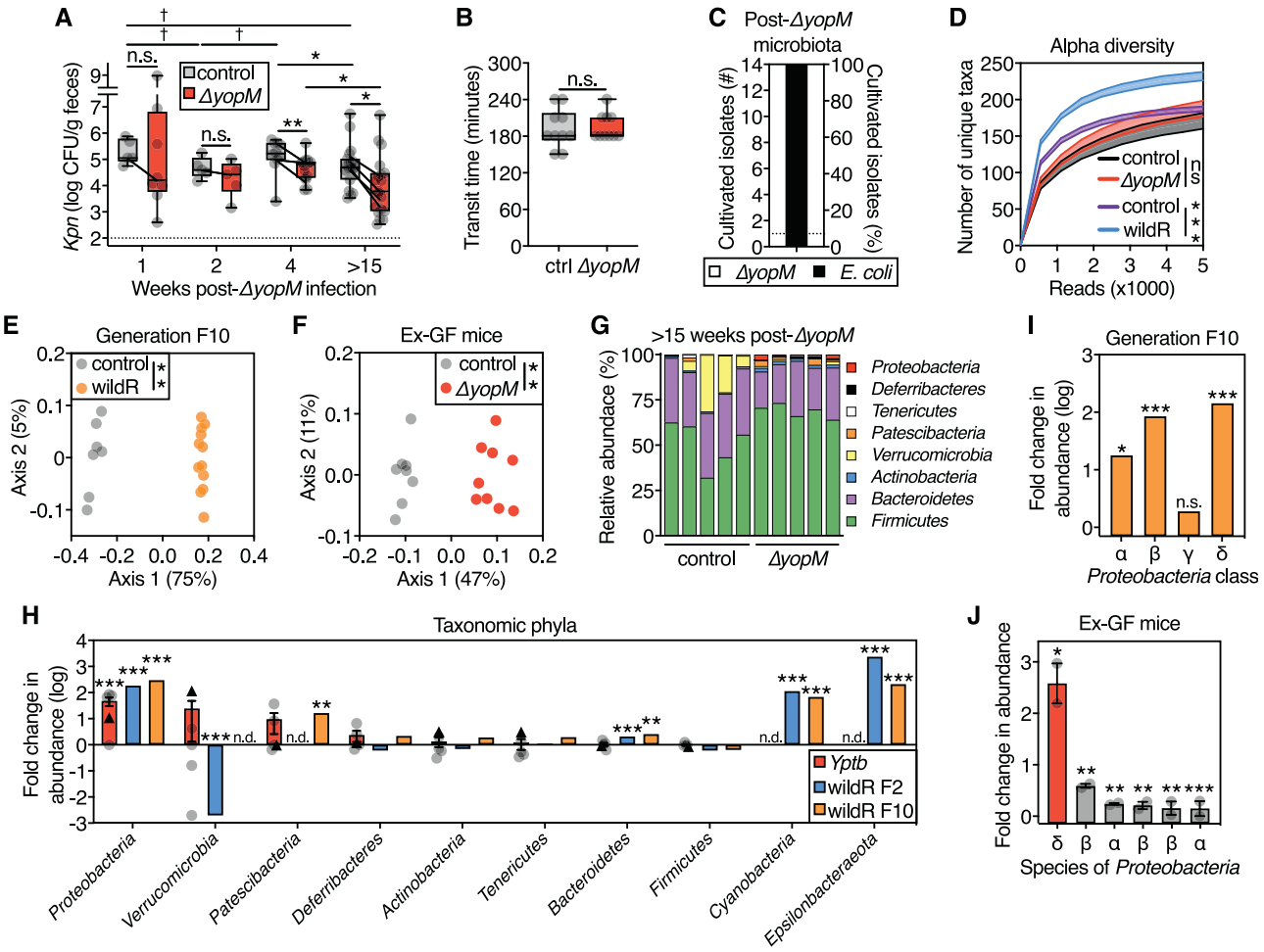

Figure S1. Infection-trained microbiota enhance colonization resistance, related to Figure 1

(A) *Kpn* CFU in the feces of control and post-*ΔyopM* mice at 1, 2, 4, and >15 weeks post-*ΔyopM* infection. The 1 and 2 week time points represent single experiments (n = 5-8). The 4 and >15 week time points are reproduced from Figure 1E. Lines connect the medians of paired cages.

(B) Time for a gavaged dye to transit through the gut of control and post-*ΔyopM* mice at >15 weeks post-*ΔyopM* infection (1 experiment with 2 paired cages, n = 10).

(C) Identity of isolates cultured (on MacConkey agar at 25°C) from the microbiota of mice at >15 weeks post-*ΔyopM* infection. The dotted line indicates the detection limit (1 in 14 or 7% of isolates).

(D) Number of unique 16S sequences identified in the gut microbiota of post-*ΔyopM*, F2 wildR, and respective control mice as a function of read depth. Lines represent mean ± SEM (n = 11-20, with 10 iterations averaged per n).

(E and F) PCoA plots of unweighted UniFrac distances between the 16S profiles of (E) control and F10 wildR mice (n = 7-12) and (F) ex-GF mice conventionalized with control or post-*ΔyopM* microbiota (n = 8-9). Percentages represent the variance explained by each PC.

(G) Relative abundance of phyla in the gut microbiota of control and post-*ΔyopM* mice at >15 weeks post-*ΔyopM* infection. Data are representative of 4 experiments.

(H) Fold change in the median abundance of phyla in the gut microbiota of post-*Yptb* (circles, *Yptb ΔyopM*; triangles, *Yptb* WT; n = 23-27), F2 wildR (n = 11-12), and F10 wildR (n = 7-12) versus respective control mice. Post-*Yptb* bars show mean ± SEM of 5 paired cages. Only fold changes > 2 were considered significant. n.d., not detected.

(I) Fold change in the median abundance of *Proteobacteria* classes (indicated by Greek letters) in the gut microbiota of F10 wildR versus control mice (n = 7-12).

(J) Fold change in the median abundance of *Proteobacteria* species (classes indicated by Greek letters) in the gut microbiota of ex-GF mice conventionalized with post-*ΔyopM* versus control microbiota. Bars show mean ± SEM of 2 paired cages (n = 8-9). Colors indicate engraftment (gray, negative; red, positive in post-*ΔyopM* versus control). Only *Proteobacteria* species with $p < 0.05$ are displayed.

The control for post-*Yptb* (*ΔyopM* and WT) and F10 wildR mice was naive SPF mice. The control for F2 wildR mice was F2 labR mice. n.s., not significant; †$p < 0.1$; *$p < 0.05$; **$p < 0.01$; ***$p < 0.001$ by Mann-Whitney test (A, B, J; in H-I, with Benjamini-Hochberg correction), Kruskal-Wallis test (D), or PERMANOVA (E-F).

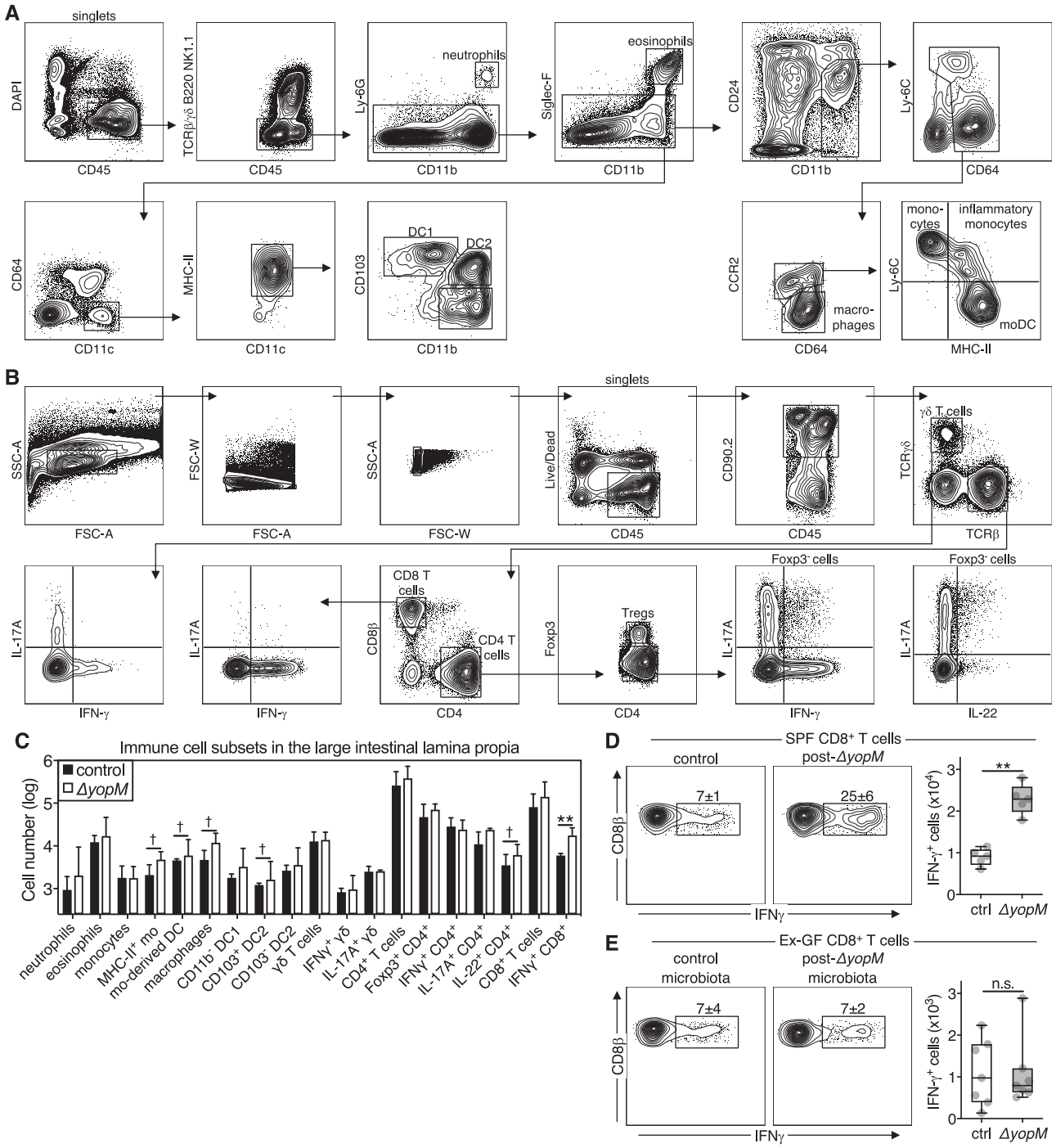

Figure S2. Gut immunity of post-*ΔyopM* mice, related to Figure 1

(A and B) Gating strategy for (A) innate immune and (B) T cells. DC, dendritic cell; moDC, monocyte-derived DC; Tregs, regulatory T cells; IFN, interferon; IL, interleukin.

(C) Numbers of innate immune cells, total T cells, and cytokine-producing T cells (restimulated with PMA/ionomycin) in the large intestinal (cecum and colon) lamina propria of control and post-*ΔyopM* mice at 4-5 weeks post-*ΔyopM* infection. Bars show median ± 95% confidence intervals (n = 5). Data either represent 1 experiment (innate immune cells) or are representative of 2 experiments (T cells).

(D and E) IFNγ-producing $CD8^+$ T cells in (D) SPF control and post-*ΔyopM* mice and (E) ex-GF mice conventionalized with control or post-*ΔyopM* microbiota. Left: Numbers in representative contour plots indicate mean frequency ± SEM. Right: Data either (D) are representative of 2 experiments or (E) represent 1 experiment with 2 paired cages (n = 7).

n.s., not significant; †$p < 0.1$; **$p < 0.01$ by Student's t test (C-E).

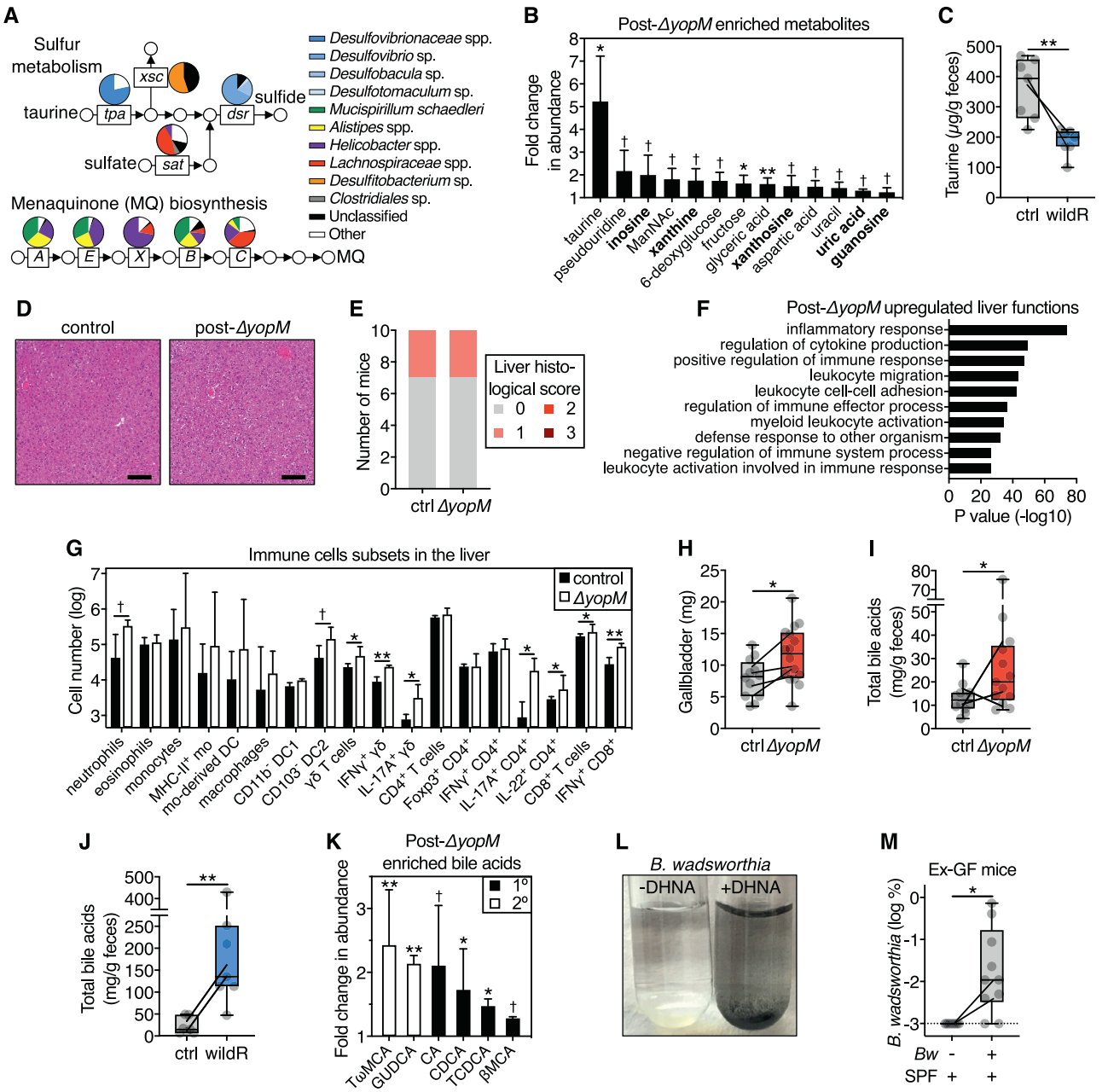

Figure S3. Infection-trained microbiota are enriched for taurine-utilizing taxa, related to Figure 2

(A) Pathways enriched in the F2 wildR shotgun metagenome. Pie charts represent the relative contribution of taxa to a function. Abbreviations same as in Figure 2D.

(B) Fold change in the median abundance of metabolites enriched in the cecal contents of post-*ΔyopM* versus control mice at >15 weeks post-*ΔyopM* infection. Bars show mean ± SEM of 3 paired cages (n = 13-14). Metabolites in bold are related to xanthine oxidase.

(C) Abundance of taurine in the cecal contents of F10 wildR mice (1 experiment with 2 paired cages, n = 7, fold decrease = 2).

(D and E) (D) Representative micrographs and (E) histological score of liver sections from control and post-*ΔyopM* mice at 4 weeks post-*ΔyopM* infection. Scale bar, 100 μm.

(F) Top 10 most enriched functions (GO terms) among genes upregulated ($\log_2$ fold change > 0.5, p < 0.1 by Wald test with Benjamini-Hochberg correction) in the livers of post-*ΔyopM* versus control mice at 4-5 weeks post-*ΔyopM* infection.

(G) Numbers of innate immune cells, total T cells, and cytokine-producing T cells (restimulated with PMA/ionomycin) in the livers of control and post-*ΔyopM* mice at 4-5 weeks post-*ΔyopM* infection. Bars show median ± 95% confidence intervals (n = 5). Data either represent 1 experiment (innate immune cells) or are representative of 2 experiments (T cells). Gating strategies and abbreviations same as in Figure S2.

(H) Weights of gallbladders from control and post-*ΔyopM* mice at >4 weeks post-*ΔyopM* infection (4 pooled experiments, n = 12-16, fold increase = 1.4).

(legend continued on next page)

(I) Abundance of total bile acids in the feces of control and post-*ΔyopM* mice at >15 weeks post-*ΔyopM* infection (3 pooled experiments, n = 12-13, fold increase = 1.5).
(J) Abundance of total bile acids in the feces of control and F10 wildR mice (1 experiment with 2 paired cages, n = 7, fold increase = 9.3).
(K) Fold change in the median abundance of individual bile acids enriched in the cecal contents of post-*ΔyopM* versus control mice at >15 weeks post-*ΔyopM* infection. Bars show mean ± SEM of 3 paired cages (n = 12-14). 1°, primary bile acids; 2°, secondary bile acids; TωMCA; tauro-ω-muricholic acid; GUDCA, glycoursodeoxycholic acid; CA, cholic acid; CDCA, chenodeoxycholic acid; TCDCA, taurochenodeoxycholic acid; βMCA, β-muricholic acid.
(L) *B. wadsworthia* growth (indicated by black color) in minimal media + taurine ± DHNA + ferrous iron (reacts with sulfide to form a black precipitate).
(M) Relative abundance of *B. wadsworthia* (*Bw*) in the gut microbiota of ex-GF mice conventionalized with the microbiota of SPF mice or, prior to conventionalization, pre-engrafted with *Bw* (2 pooled experiments, n = 10, fold increase = 7.5). The dotted line indicates the detection limit.
The control for post-*ΔyopM* and F10 wildR mice was naive SPF mice. The control for F2 wildR mice was F2 labR mice. In box and whisker plots, lines connect the medians of paired cages. n.s., not significant; †$p < 0.1$; *$p < 0.05$; **$p < 0.01$ by Mann-Whitney (B, C, H-K, M), hypergeometric (F), or Student's t test (G). See also Table S4.

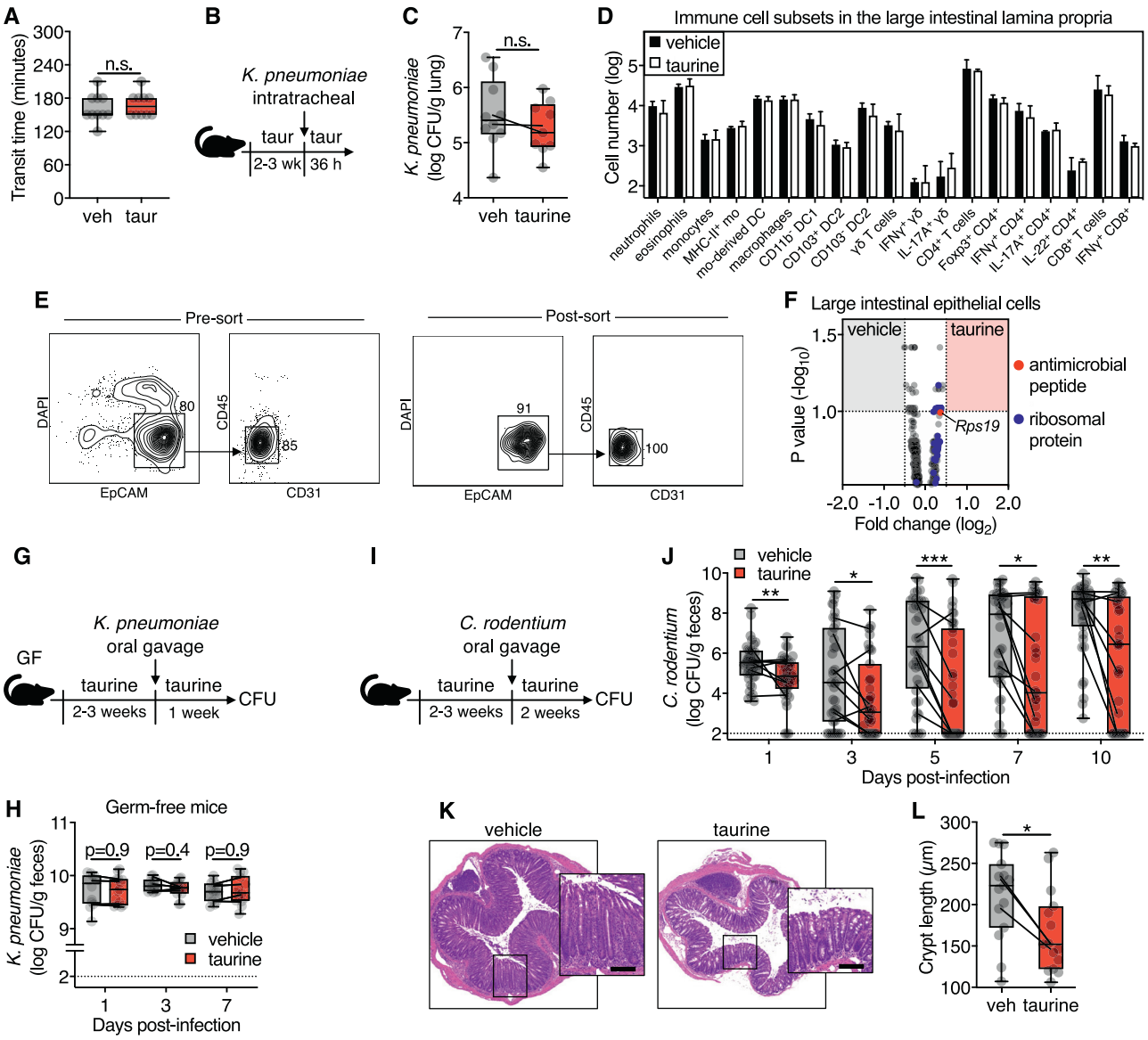

Figure S4. Taurine-trained microbiota enhances colonization resistance, related to Figure 3

(A) Time for a gavaged dye to transit through the gut of vehicle and taurine-treated mice (1 experiment with 2 paired cages, n = 10).

(B) Mice were maintained on taurine after intratracheal inoculation with *Kpn*.

(C) *Kpn* CFU in the lungs of vehicle and taurine-treated mice at 36 h post-intratracheal inoculation with *Kpn* (2 pooled experiments, n = 9-10).

(D) Numbers of innate immune cells, total T cells, and cytokine-producing T cells (restimulated with PMA/ionomycin) in the large intestinal (cecum and colon) lamina propria of vehicle and taurine-treated mice. Bars show median ± 95% confidence intervals (n = 5, all $p > 0.14$). Data are representative of 2 experiments. Gating strategies and abbreviations same as in Figure S2.

(E) Pre-sort: Gating strategy to sort epithelial cells from the large intestines of vehicle and taurine-treated mice. Post-sort: Representative contour plots depicting the purity of sorted epithelial cells. Both pre and post-sort are gated on singlets. Numbers represent population frequency.

(F) Differentially expressed genes in large intestinal epithelial cells sorted from taurine versus vehicle-treated mice (2 pooled experiments, n = 6-7). Horizontal dotted line, corrected $p = 0.1$; vertical dotted lines, $\log_2$ fold change = 0.5. Points in the red and gray areas represent genes up and downregulated in taurine, respectively. Only genes with $p < 0.3$ are displayed. The annotated antimicrobial peptide (*Rps19*) has $p = 0.102$.

(G) GF mice were maintained on taurine after *Kpn* infection.

(H) *Kpn* CFU in the feces of vehicle and taurine-treated GF mice (2 pooled experiments, n = 13-15).

(I) SPF mice were maintained on taurine after *C. rodentium* infection.

(J) *C. rodentium* CFU in the feces of vehicle and taurine-treated mice (5 pooled experiments, n = 39-40).

(K and L) (K) Transverse colonic sections and (L) quantification of colonic crypt lengths of vehicle and taurine-treated mice at 14 days post-*C. rodentium* infection (2 pooled experiments, n = 15, fold decrease = 1.5). Scale bar, 100 μm.

In box and whisker plots, lines connect the medians of paired cages. n.s., not significant; *$p < 0.05$; **$p < 0.01$; ***$p < 0.001$ by Mann-Whitney (A, C, J, H, L), Student's *t* (D), or Wald test (F, with Benjamini-Hochberg correction). See also Table S4.

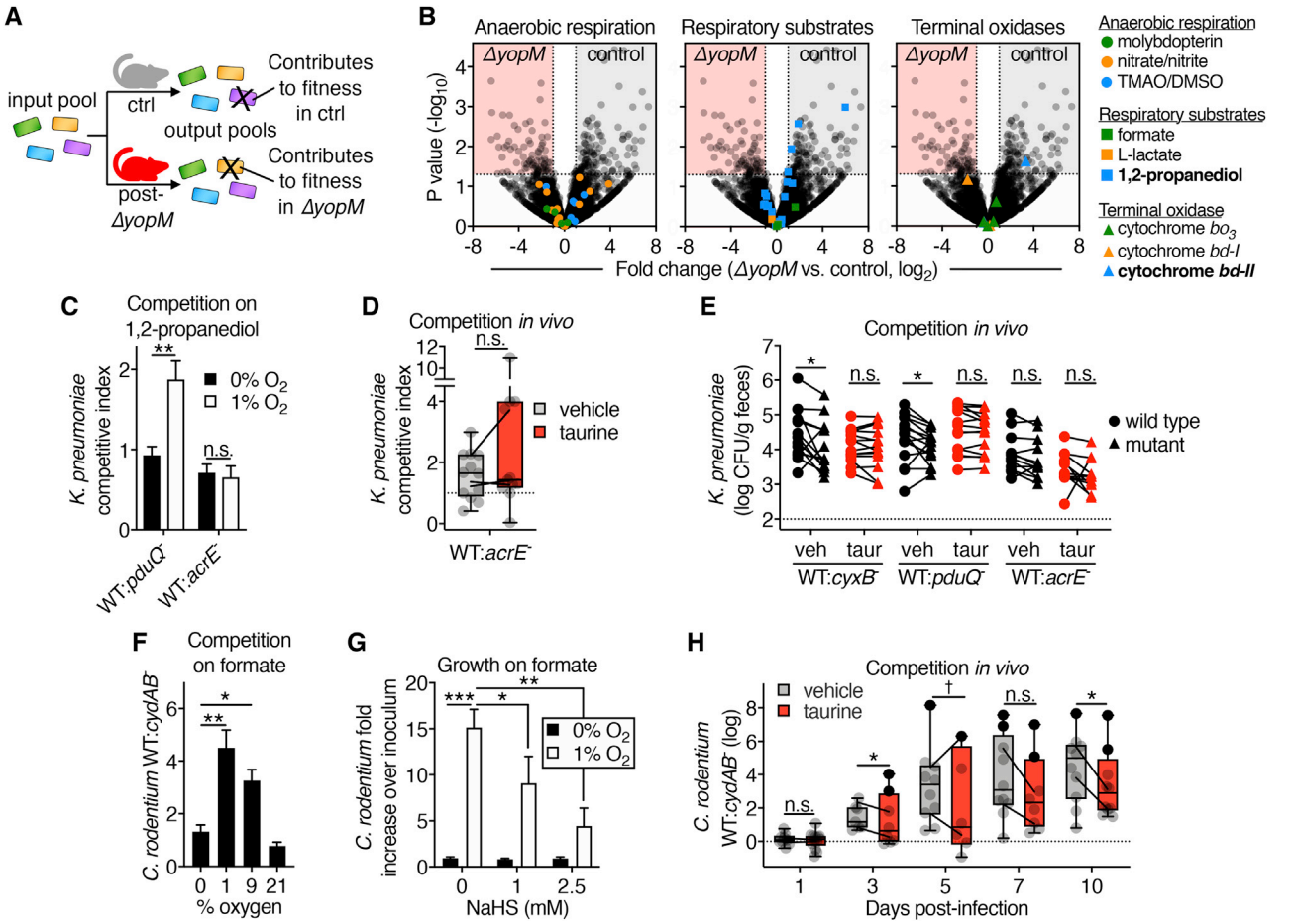

Figure S5. Taurine-derived sulfide inhibits pathogen respiration, related to Figure 4

(A) A pool of *Kpn* transposon mutants was passaged through control and post-*ΔyopM* mice. Genes in which mutants were preferentially depleted (X) from the output of control or post-*ΔyopM* mice contributed to fitness in that condition.

(B) *Kpn* genes that differentially contribute to fitness in post-*ΔyopM* versus control mice. Highlighted genes mediate respiration with anaerobic electron acceptors (left panel, circles), utilization of non-fermentable substrates (middle panel, squares), or respiration with oxygen (right panel, triangles). Data represent 2 pooled experiments (n = 6-7 samples per group). Horizontal dotted line, p = 0.05; vertical dotted lines, $\log_2$ fold change = 1. Points in the gray and red areas represent genes that contribute to fitness in control and post-*ΔyopM* mice, respectively.

(C) The CI of *Kpn* WT:*pduQ*$^-$ and WT:*acrE*$^-$ after growth on 1,2-propanediol ± oxygen (2 pooled experiments, n = 6).

(D) The CI of *Kpn* WT:*acrE*$^-$ in the feces of vehicle and taurine-treated mice at 1 day post-*Kpn* infection (2 pooled experiments, n = 11-12). The dotted line indicates equal fitness between WT and mutant.

(E) Paired CFU of the *Kpn* WT (circles) and the *cyxB*$^-$, *pduQ*$^-$, or *acrE*$^-$ mutant (triangles) in the feces of vehicle and taurine-treated mice at 1 day post-*Kpn* infection. Lines connect WT and mutant CFU within individual mice (represented as CI in Figures 4G and S5C). The dotted line indicates the detection limit.

(F) The CI of the *C. rodentium* WT and *cydAB*$^-$ mutant after growth on formate ± oxygen (2 pooled experiments, n = 6).

(G) Fold increase in *C. rodentium* CFU after growth on formate ± sodium hydrosulfide (NaHS) (3 pooled experiments, n = 8).

(H) The CI of *C. rodentium* WT:*cydAB*$^-$ in the feces of vehicle and taurine-treated mice (2 pooled experiments, n = 10). The CI for mice with < 10 detectable CFU were excluded. Outliers (black points) were identified using the ROUT method (Q = 0.1%) and excluded when determining significance. Lines connect the medians of paired cages. The dotted line indicates equal fitness between WT and mutant.

Bars show mean ± SEM. n.s., not significant; †p < 0.1; *p < 0.05; **p < 0.01; ***p < 0.001 by Mann-Whitney (C, D, F-H), Wald (B), or Wilcoxon matched-pairs signed-rank test (D).